

IMPROVING GALACTIC CENTER ASTROMETRY BY REDUCING THE EFFECTS OF GEOMETRIC DISTORTION

S. YELDA¹, J. R. LU², A. M. GHEZ^{1,3}, W. CLARKSON^{1,6}, J. ANDERSON⁴, T. DO⁵, AND K. MATTHEWS²

¹ Department of Physics and Astronomy, UCLA, Los Angeles, CA 90095-1547, USA; syelda@astro.ucla.edu, ghez@astro.ucla.edu, clarkson@astro.ucla.edu

² Department of Astrophysics, California Institute of Technology, MC 249-17, Pasadena, CA 91125, USA; jlu@astro.caltech.edu, kym@caltech.edu

³ Institute of Geophysics and Planetary Physics, UCLA, Los Angeles, CA 90095-1565, USA

⁴ Space Telescope Science Institute, 3700 San Martin Drive, Baltimore, MD 21218, USA; jayander@stsci.edu

⁵ Department of Physics and Astronomy, UC Irvine, Irvine, CA 92697, USA; tdo@astro.ucla.edu

Received 2010 September 9; accepted 2010 September 24; published 2010 November 18

ABSTRACT

We present significantly improved proper motion measurements of the Milky Way’s central stellar cluster. These improvements are made possible by refining our astrometric reference frame with a new geometric optical distortion model for the W. M. Keck II 10 m telescope’s adaptive optics camera (NIRC2) in its narrow field mode. For the first time, this distortion model is constructed from on-sky measurements and is made available to the public in the form of FITS files. When applied to widely dithered images, it produces residuals in the separations of stars that are a factor of ~ 3 smaller compared with the outcome using previous models. By applying this new model, along with corrections for differential atmospheric refraction, to widely dithered images of SiO masers at the Galactic center (GC), we improve our ability to tie into the precisely measured radio Sgr A*-rest frame. The resulting infrared reference frame is ~ 2 – 3 times more accurate and stable than earlier published efforts. In this reference frame, Sgr A* is localized to within a position of 0.6 mas and a velocity of 0.09 mas yr^{-1} , or $\sim 3.4 \text{ km s}^{-1}$ at 8 kpc (1σ). Also, proper motions for members of the central stellar cluster are more accurate, although less precise, due to the limited number of these wide field measurements. These proper motion measurements show that, with respect to Sgr A*, the central stellar cluster has no rotation in the plane of the sky to within $0.3 \text{ mas yr}^{-1} \text{ arcsec}^{-1}$, has no net translational motion with respect to Sgr A* to within 0.1 mas yr^{-1} , and has net rotation perpendicular to the plane of the sky along the Galactic plane, as has previously been observed. While earlier proper motion studies defined a reference frame by assuming no net motion of the stellar cluster, this approach is fundamentally limited by the cluster’s intrinsic dispersion and therefore will not improve with time. We define a reference frame with SiO masers and this reference frame’s stability should improve steadily with future measurements of the SiO masers in this region ($\propto t^{-3/2}$). This is essential for achieving the necessary reference frame stability required to detect the effects of general relativity and extended mass on short-period stars at the GC.

Key words: astrometry – Galaxy: kinematics and dynamics – instrumentation: adaptive optics

Online-only material: color figures, machine-readable table

1. INTRODUCTION

High angular resolution astrometry has been a powerful technique for studies of the Galactic center (GC). Over the last decade, it has revealed a supermassive black hole (Eckart & Genzel 1997; Ghez et al. 1998), a disk of young stars surrounding the central supermassive black hole (Levin & Beloborodov 2003; Genzel et al. 2003; Paumard et al. 2006; Lu et al. 2009), and allowed for measurements of the orbit about the GC of the Arches, a massive young star cluster located at a projected galactocentric distance of 30 pc (Stolte et al. 2008; W. Clarkson et al. 2011, in preparation). While the speckle imaging work carried out on the GC in 1990s had typical centroiding uncertainties of ~ 1 mas, recent deep, adaptive optics (AO) images have improved the precision of stellar centroiding by a factor of ~ 6 – 7 , significantly increasing the scientific potential of astrometry at the GC (Ghez et al. 2008; Gillessen et al. 2009b). Further gains in astrometric precision would allow ultra-precise measurements of the distance to the GC (R_o), measurements of individual stellar orbits at larger galactocentric radii, and, more ambitiously, measurements of post-Newtonian effects in the orbits of short-period stars (e.g., Jaroszyński 1998, 1999; Salim & Gould 1999; Fragile & Mathews 2000; Rubilar &

Eckart 2001; Weinberg et al. 2005; Zucker & Alexander 2007; Kraniotis 2007; Nucita et al. 2007; Will 2008). Such gains will also probe the possibility that the supermassive black hole is moving with respect to the central stellar cluster, either due to the gravitational influence of a massive companion or from a systematic effect produced by improper alignment of images.

Two factors that currently limit astrometric measurements of stars at the GC are (1) the level to which AO cameras’ geometric distortions are known and (2) differential atmospheric refraction (DAR), which has not yet been explicitly corrected for in any GC proper motion study (Ghez et al. 2008; Gillessen et al. 2009b). While optical distortion from an infrared camera is expected to be static, distortion from the AO system and the atmosphere not corrected by AO is not. Initial estimates of the optical distortions for AO cameras are generally based on either the optical design or laboratory test, which do not perfectly match the actual optical distortion of the system. Both uncorrected camera distortions and DAR leave ~ 1 – 5 mas scale distortions over the spatial scales of the SiO masers that are used to define the Sgr A*-radio rest frame for proper motions of stars at the GC (see, e.g., Reid et al. 2007). These are significantly larger than the ~ 0.2 – 0.3 mas precision achieved in the relative astrometry of Ghez et al. (2008) and Gillessen et al. (2009b). The impact of all these effects on relative astrometry has been minimized by mapping the coordinate systems of different

⁶ Current address: Department of Astronomy, Indiana University, 727 East 3rd Street, Swain West 319, Bloomington, IN 47405-7105, USA

epochs of observations to a reference frame using high-order transformations, allowing $\sim 0.2\text{--}0.3$ mas precision in the relative astrometry to be achieved. However, the full impact of these effects is imposed on astrometric measurements in a reference frame that is known to be at rest with respect to Sgr A*-radio (henceforth, the Sgr A*-radio rest frame). Therefore, correcting these effects would have the greatest improvement on astrometric measurements in the maser frame. Relative astrometry would also be improved by eliminating these effects before the images, which are obtained at different times and occasionally different orientations, are combined.

In this paper, we improve the astrometric accuracy and precision of Keck AO measurements of the GC by (1) deriving a new, publicly available distortion solution for the infrared imaging camera behind the Keck AO system (NIRC2) and (2) correcting for DAR. Furthermore, having corrected for these effects, we show that an astrometric reference frame for the GC can now be established with Sgr A* at rest to within 0.09 mas yr^{-1} (3.4 km s^{-1} at the distance to the GC), thereby improving the stability of the reference frame. Section 2 presents observations and analysis of the globular cluster, M92, that were used to derive the first distortion solution for NIRC2 that is based upon on-sky measurements, as opposed to NIRC2's internal pinhole mask. We also discuss the observations and analysis of GC data used to illustrate the impact of our technical work here. We present the results and tests of the distortion solution in Section 3.1. In Section 4.1, we apply this solution, along with corrections for DAR, to observations of the GC and report the positions and proper motions of a set of infrared astrometric standards ($N \sim 10^3$) in an Sgr A*-radio rest frame. In Section 4.3, we measure the motion of the stellar cluster in this reference frame and show that these stars exhibit significant net motion in the plane of the Galaxy. Finally, we consider the implications of this work for measuring relativistic and extended mass effects on short-period stars. While this work has been carried out in the context of the GC, the new distortion solution also benefits a wide array of other science that is currently being carried out with NIRC2, including astrometric studies of extrasolar planets (Marois et al. 2008), brown dwarf binaries (Konopacky et al. 2007; Liu et al. 2008; Dupuy et al. 2009), compact objects (Cameron & Kulkarni 2007), and external galaxies (e.g., Max et al. 2005).

2. OBSERVATIONS AND ANALYSIS

In this section, we report all the new observations and analysis carried out for this paper. Section 2.1 discusses the observations of M92 that are used to create a new NIRC2 distortion model presented in Section 3.1. Section 2.2 describes the observations of the GC that are used to test the new distortion model in Section 3.2 and to generate a new IR astrometric reference frame at the GC in Section 4.1.

2.1. M92

To characterize the optical distortion in the NIRC2 camera, it is ideal to compare the measured set of stellar positions to those in a distortion-free reference frame. As this idealized reference frame does not exist, we choose observations of M92 (NGC 6341; $\alpha = 17 \ 17 \ 07.27$, $\delta = +43 \ 08 \ 11.5$) made with the well-characterized Advanced Camera for Surveys Wide Field

Channel (ACS/WFC) on the *Hubble Space Telescope* (HST), which has a plate scale $\sim 49.9933 \pm 0.0005 \text{ mas pixel}^{-1}$ and position angle (P.A.) offset $= -0^\circ.0006 \pm 0^\circ.0023$ (van der Marel et al. 2007), as our reference frame. The static distortion in this camera has been corrected down to the ~ 0.01 pixel (~ 0.5 mas) level (Anderson 2005, 2007; Anderson & King 2006) and is therefore a useful reference for our purposes given the level of distortion in the NIRC2 camera. While several clusters were considered during the planning phase of this project, M92 was chosen because it had been extensively observed with ACS/WFC, was observable in the northern hemisphere during the summer, was sufficiently crowded, and had an isolated natural guide star (NGS) available. The HST observations of M92 used for this analysis were made on 2006 April 11 with both the F814W (I) and F606W (V) filters as part of the ACS Survey of Globular Clusters (GO-10775, PI: A. Sarajedini). The details of the observations and data reduction can be found in Anderson et al. (2008), and the catalog of positions was provided in advance of publication by J. Anderson. We used the Anderson (2007) correction for the linear skew in ACS to ensure that our reference frame was free of skew.

Observations of M92 were made from 2007 June to 2009 May using the AO system on the W. M. Keck II 10 m telescope with the facility near-infrared camera NIRC2 (PI: K. Matthews). Aside from the 2007 July data set, these observations were obtained upon completion of our primary science program for the night (GC astrometry), or when conditions were not optimal for the primary science program (e.g., clouds were present or seeing was relatively poor). All images were taken with the narrow field camera, which maps the 1024×1024 pixel array into $\sim 10'' \times 10''$ field of view, and through the K' ($\lambda_0 = 2.12 \ \mu\text{m}$, $\Delta\lambda = 0.35 \ \mu\text{m}$) bandpass filter. While the natural guide star adaptive optics (NGSAO) system was used to obtain the majority of the data, the laser guide star (LGS) AO system was used for one run in 2008 June. The NGSAO atmospheric corrections and the LGSAO low-order, tip-tilt corrections were made using visible observations of USNO-B1.0 1331-0325486 ($R = 8.5$ mag). The resulting image point-spread functions (PSFs) had Strehl ratios of ~ 0.55 and FWHM of ~ 50 mas, on average.

M92 was observed at 79 different combinations of P.A.s) and offsets (see Figure 1), with three identical exposures taken at each pointing. This allowed for a given star to fall on several different parts of the detector over the course of the observations. We note for clarity that the reported P.A. value is the angle (eastward) of the camera's columns with respect to north. The field of view of NIRC2's narrow camera contained the NGS in each pointing, and in most cases two other nearby stars, which are circled in Figure 2; this facilitated the process of combining the positional information from all of the different pointings. Table 1 provides the details of the NIRC2 M92 observations.

The M92 images are calibrated and stellar positions are measured from these images using standard techniques. Specifically, the images are first dark- and sky-subtracted, flat-fielded, and bad-pixel and cosmic-ray-corrected. The images are then run through the PSF fitting program *StarFinder* (Diolaiti et al. 2000), which is optimized for AO observations of crowded stellar fields to identify and characterize stars in the field of view. *StarFinder* iteratively constructs a PSF from a set of bright stars in the field, which have been pre-selected by the user. For M92, a total of 16 stars spread out across the detector are used to obtain a PSF that is representative of the entire field. The resulting PSF is then cross-correlated with the image and detections with a

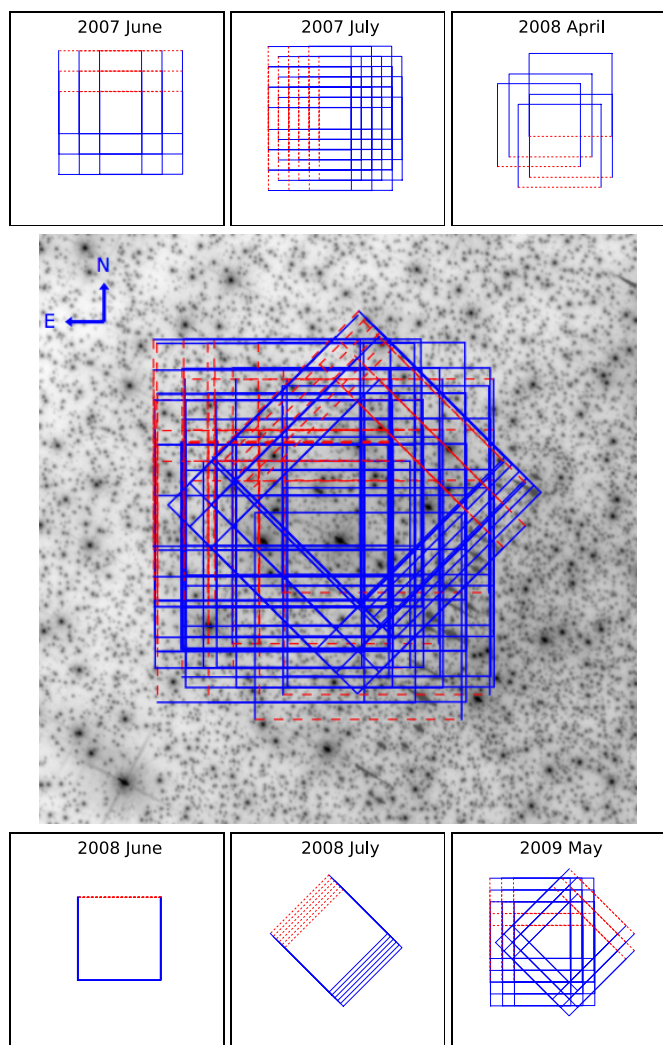


Figure 1. ACS/WFC image with the 79 NIRC2 pointings. The red dashed side of each NIRC2 box denotes the top of the detector's field of view. Each NIRC2 field is $10'' \times 10''$, while the ACS image shown is $\sim 30'' \times 30''$. The pattern for the individual epochs' exposures is shown in the insets.

(A color version of this figure is available in the online journal.)

correlation peak of at least 0.7 are considered candidate stars. Relative astrometry and photometry are extracted by fitting the PSF to each candidate star. This results in a star list, which contains the NIRC2 pixel coordinates for the detected stars, for each of the 237 images.

Final star lists for each pointing are produced by combining each set of three star lists from images with the same observational setup. Positions are taken from the first of the three images and the centroiding uncertainties are estimated empirically using the three images at each pointing and computing the rms error of each star's position.⁷ The median centroiding uncertainty is ~ 0.035 pixel (~ 0.35 mas; see Figure 3). Two initial criteria are used to trim out false or problematic source detections. First, only stars detected in all three images are kept. Second, we remove the two brightest stars (the NGS and a comparably bright star $\sim 5'$ to the east that appears in the images of 147 out of 237 pointings) and any other source identified within a 60 pixel ($\sim 0.6'$) radius of these stars (see Figure 2).

⁷ Choosing positions from the first of the three images was unintentional, but should not affect the results since the centroiding uncertainties are smaller than the level of distortion in the images.

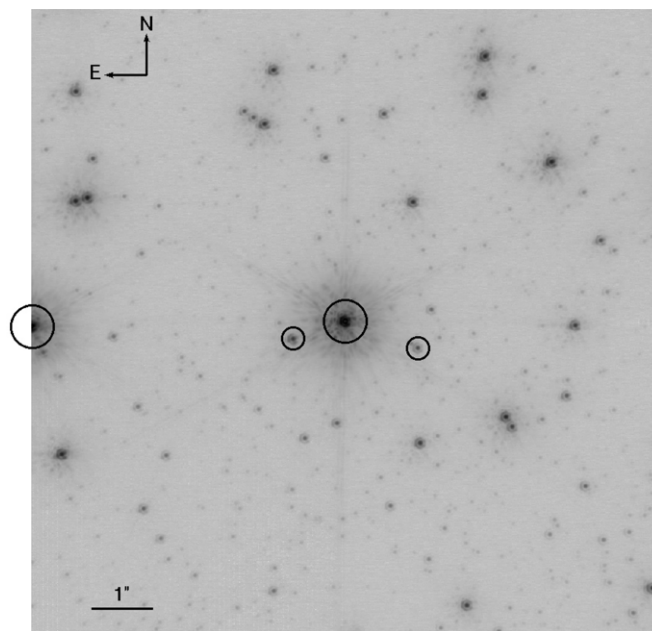


Figure 2. Diffraction-limited NGSAO NIRC2 image of one of the M92 fields used to characterize the optical distortion in the NIRC2 camera. The circled stars at the center of the image, the NGS and two fainter stars, are present in most of the M92 NIRC2 observations and are used to register the images, each of which had a different position/orientation on the sky. The NGS and the circled star $\sim 5''$ to its east were almost always (i.e., when clouds were not present) detected at levels that saturated the detector and were therefore removed from the analysis (see Section 2).

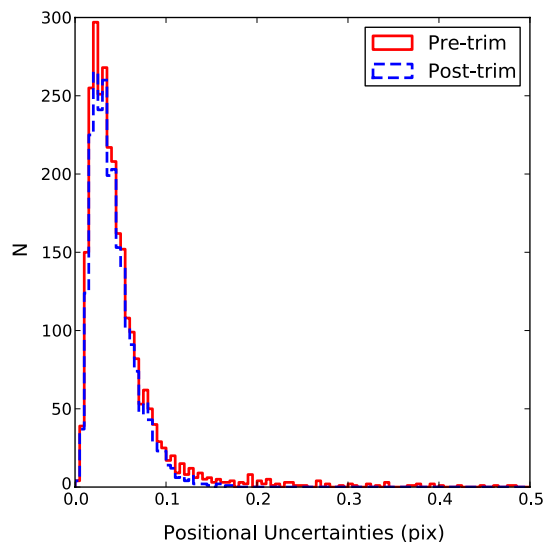


Figure 3. Histogram of NIRC2 (plate scale ~ 10 mas pixel⁻¹) positional uncertainties for stars matched to the ACS/WFC star list before (solid red) and after (dashed blue) removing all outliers (see the text). The uncertainties are calculated from the rms error of the positions obtained from three images taken at the same position on the sky. The distributions peak at ~ 0.02 pixel.

(A color version of this figure is available in the online journal.)

These two sources are ~ 1 mag brighter than any other detected star and are often detected at levels that saturate the detector. Saturation leads to poor PSF matching with the empirical PSF estimate, and consequently poor positional estimates for these two stars, as well as ~ 20 – 50 false detections in their halos. With these selection criteria, the 79 final star lists contain a combined total of 3846 stellar position measurements of more than 150 independent stars.

Table 1
Summary of M92 Images

Date ^a (UT)	P.A. (deg)	(X, Y) _{GS} ^b (pixel)	Δ(X, Y) ^c (pixel)	El (deg)	Temp (K)	Pressure (mbar)	RH ^d (%)	ΔR ^e (mas)	t _{exp,i} × Co-add (s)	(FWHM) (mas)	(Strehl)	N Stars Detected	N Stars Used	(σ _{pos}) ^f (pixel)
2007 Jun 21	0	508, 512	0, 0	53	271.2	616.8	92	2.74	3.0 × 10	49	0.55	105	69	0.037
			254, -252	53	271.1	616.7	89	2.77		48	0.55	145	58	0.035
			251, 252	52	271.1	616.7	89	2.81		48	0.57	112	46	0.045
			-251, -252	52	271.3	616.7	93	2.84		48	0.59	176	56	0.034
			-253, 250	51	271.3	616.7	93	2.89		49	0.54	110	57	0.037
			251, 0	51	271.2	616.7	95	2.93		48	0.60	124	58	0.044
			-251, -1	50	271.2	616.7	95	2.97		47	0.59	115	64	0.049
			2, -250	50	271.1	616.7	96	3.02		47	0.58	124	47	0.063
0, 253	49	271.0	616.6	97	3.07	46	0.61	94	51	0.058				
2007 Jul 29	90	457, 499	0, 0	67	272.9	615.3	11	2.07	0.8 × 60	45	0.64	73	47	0.031
			255, -251	67	272.9	615.3	11	2.07		45	0.72	53	38	0.048
			251, 255	67	272.9	615.3	12	2.07		45	0.68	84	41	0.042
			-249, -251	67	272.9	615.2	12	2.07		46	0.66	65	40	0.052
			-252, 251	67	272.9	615.2	13	2.07		45	0.69	132	52	0.031
			254, 2	67	272.9	615.3	13	2.07		45	0.71	72	44	0.021
			-252, 0	66	272.9	615.2	13	2.08		45	0.72	93	48	0.037
			3, -250	66	272.8	615.2	12	2.09		44	0.73	69	47	0.029
			-2, 253	66	272.8	615.2	12	2.10		45	0.72	92	51	0.024
			-125, -124	65	272.8	615.2	12	2.11		45	0.72	85	50	0.026
			128, -375	65	272.8	615.2	13	2.12		45	0.73	89	48	0.030
			126, 129	65	272.8	615.2	12	2.14		45	0.70	84	54	0.030
			-374, -376	64	272.8	615.2	13	2.16		46	0.69	47	33	0.033
			-378, 126	64	272.8	615.2	12	2.18		46	0.68	74	39	0.067
			128, -123	63	272.9	615.2	12	2.20		46	0.67	77	49	0.038
			-374, -125	62	272.9	615.2	12	2.22		46	0.67	72	38	0.032
			-121, -374	62	272.9	615.2	12	2.25		46	0.67	51	38	0.028
			-127, 129	61	273.0	615.2	11	2.27		46	0.66	87	45	0.045
			127, -121	60	273.1	615.1	11	2.31		46	0.65	81	47	0.045
			380, -373	60	273.2	615.1	12	2.34		47	0.63	52	33	0.071
378, 132	59	273.1	615.1	12	2.38	46	0.65	51	39	0.025				
-126, -373	58	273.3	615.1	12	2.41	46	0.66	54	36	0.032				
-128, 130	57	273.3	615.1	11	2.46	47	0.65	76	45	0.031				
381, -120	56	273.3	615.0	11	2.50	47	0.64	43	35	0.040				
-127, -120	56	273.4	615.0	10	2.55	47	0.61	64	43	0.022				
129, -371	55	273.3	615.0	12	2.60	47	0.63	54	39	0.040				
124, 133	54	273.3	614.9	11	2.66	48	0.60	79	47	0.036				
2008 Apr 28	180	496, 477	0, 0	67	271.0	615.8	82	2.08	0.8 × 60	47	0.56	31	20	0.022
			252, -252	67	271.0	615.7	81	2.08		48	0.53	32	0	-1.000
			248, 253	67	271.0	615.8	83	2.08		48	0.55	55	15	0.061
			113, -375	63	271.5	616.0	70	2.23		48	0.54	12	0	-1.000
			-143, -120	59	271.0	616.0	77	2.39		51	0.44	13	9	0.022
2008 Jun 3	0	776, 573	0, 0	42	273.3	616.0	64	3.85	1.5 × 6	50	0.47	30	0	-1.000
			4, 4	42	273.2	616.1	65	3.89		51	0.48	32	0	-1.000
			-4, 0	42	273.2	616.1	65	3.93		58	0.29	29	0	-1.000
			4, 0	41	273.2	616.1	65	3.97		54	0.38	32	0	-1.000
			-4, 3	41	273.2	616.1	65	4.01		54	0.38	25	0	-1.000
			-5, -4	41	273.2	616.1	65	4.05		54	0.40	26	0	-1.000
2008 Jul 24	45	173, 565	0, 0	50	271.6	617.2	39	3.03	2.8 × 10	66	0.35	128	32	0.077
			0, -49	49	271.6	617.2	39	3.07		63	0.35	110	35	0.068
			0, -100	49	271.6	617.1	39	3.11		72	0.30	88	30	0.065
			1, -149	48	271.6	617.1	39	3.16		72	0.29	89	30	0.089
			3, -199	48	271.6	616.9	39	3.21		51	0.46	131	45	0.065
			2, -249	47	271.6	616.9	39	3.26		86	0.22	89	21	0.067
2009 May 9	0	910, 668	0, 0	66	270.6	614.6	36	2.11	0.8 × 60	52	0.45	18	10	0.072
			1, -153	66	270.6	614.6	36	2.12		49	0.50	19	15	0.031
			3, -304	65	270.6	614.6	36	2.13		49	0.47	19	16	0.026
			-154, -2	65	270.5	614.6	36	2.14		51	0.48	25	17	0.036
			-153, -154	65	270.5	614.7	36	2.15		47	0.58	30	25	0.036
			-152, -305	64	270.5	614.7	36	2.16		50	0.47	27	22	0.038
			-305, -4	64	270.8	614.7	35	2.17		50	0.51	23	19	0.034
			-305, -155	64	271.0	614.7	35	2.18		56	0.38	26	12	0.041
			-302, -306	63	271.0	614.7	35	2.20		63	0.30	22	13	0.033

Table 1
(Continued)

Date ^a (UT)	P.A. (deg)	(X, Y) _{GS} ^b (pixel)	$\Delta(X, Y)$ ^c (pixel)	El (deg)	Temp (K)	Pressure (mbar)	RH ^d (%)	ΔR ^e (mas)	$t_{\text{exp},i} \times \text{Co-add}$ (s)	(FWHM) (mas)	(Strehl)	N Stars Detected	N Stars Used	$\langle \sigma_{\text{pos}} \rangle$ ^f (pixel)
2009 May 9	90	365, 411	0, 0	62	270.8	614.6	35	2.27	0.8×60	49	0.49	25	19	0.025
			2, -153	61	270.8	614.6	35	2.29		50	0.48	24	17	0.028
			0, -302	61	270.8	614.5	35	2.31		50	0.47	10	8	0.031
			-151, -1	60	270.8	614.5	35	2.33		50	0.48	28	19	0.061
			-152, -154	60	270.8	614.5	36	2.35		47	0.56	29	22	0.035
			-149, -304	59	270.8	614.5	36	2.37		46	0.67	26	20	0.020
			-302, -4	59	270.6	614.5	36	2.40		46	0.61	35	24	0.023
			-304, -156	58	270.7	614.5	34	2.42		46	0.64	29	26	0.025
			-301, -305	58	270.7	614.5	34	2.45		48	0.53	18	15	0.030
2009 May 9	315	697, 499	0, 0	56	271.1	614.5	33	2.55	0.8×60	45	0.67	38	27	0.055
			2, -152	55	271.1	614.5	33	2.58		45	0.68	48	29	0.055
			0, -304	55	271.0	614.4	34	2.62		45	0.67	58	30	0.060
			-152, 0	54	270.7	614.3	35	2.66		47	0.56	35	22	0.044
			-148, -154	54	270.7	614.3	35	2.69		56	0.32	21	13	0.085
			-149, -305	53	270.7	614.3	35	2.74		50	0.45	43	18	0.078
			-300, -2	53	270.6	614.4	35	2.78		50	0.45	25	18	0.044
			-301, -154	52	270.6	614.5	35	2.82		59	0.29	21	13	0.063

Notes.^a 2008 June 3 data set taken in LGS-AO mode. All other data sets taken with NGS-AO.^b Position of guide star in first image of a given epoch.^c Positional offset of guide star in NIRC2 pixels relative to first pointing of epoch.^d Relative humidity.^e Model of DAR relative to the center of the image.^f Images thrown out are given a value of -1.0 for the average positional uncertainty (see the text for details).

2.2. Galactic Center

Two types of GC observations were obtained with the NIRC2 narrow camera and the LGS AO system at Keck. First, two sets of deep GC observations centered roughly on Sgr A* offer a test of the new distortion model because something is changed in each. In a data set from 2007 May, previously reported in Ghez et al. (2008), 103 frames were obtained with a camera orientation of P.A. = 0° (May 17) and another 20 frames were collected at P.A. = 200° (May 20). In a new data set collected on 2008 May 15, the first 22 images were obtained with the LGS AO system and the remaining 112 images were taken with the NGS AO system; the Strehl ratio was 31% and 22% for the LGS AO and NGS AO data that evening, respectively. Second, three new epochs of observations, designed to measure the relative positions of seven IR-bright SiO masers, were carried out in 2008 May, 2009 June, and 2010 May, bringing the total number of such observations to six. These observations are primarily to generate an astrometric reference frame in which Sgr A* is at rest, but are also used as an additional test of the new distortion solution. The 2008 May data set is identical to those reported in detail in Ghez et al. (2008, Appendix C) and consists of a total of 27 images, which were obtained in a widely dithered ($6'' \times 6''$) nine-point box pattern with three images at each of the nine pointing positions. The 2009 June data set differed in that we repeated the box pattern three times, resulting in a deeper image by ~ 0.5 mag, and the 2010 May data set was similar in total exposure time to the initial mode, but made a trade of less co-adds for more recorded images in an attempt to compensate for the shorter atmospheric coherence times that evening. We note that these observations were generally carried out under poorer seeing conditions than our other GC observations (see below), since the quality of the seeing is not the limiting factor in measuring the positions of the SiO masers. These observations are summarized in Table 2. USNO 0600-28577051, which is

offset by $9'4''$ E and $16'9''$ N from Sgr A*, served as the tip-tilt star for all of the LGS AO observations and as the NGS for the NGS AO observation.

All the GC images are calibrated in a similar manner to what was carried out with the M92 data sets, with a few exceptions. First, all images are corrected for DAR (see Section 3.1) and the geometric optical distortion using the new model derived in Section 3.1. Second, all the images from each epoch (and each configuration in the case of the deep central $10'' \times 10''$ observations) are combined into a final average map as described in Ghez et al. (2008). In addition, three subset images, each containing 1/3 of the data, are created for estimating centroiding uncertainties.

Astrometry was extracted using *StarFinder* (Diolaiti et al. 2000) in a similar manner as in Ghez et al. (2008), with a few minor modifications. Images from the individual pointings were analyzed with a correlation threshold of 0.9 in order to minimize spurious detections. The maser mosaics and the deep central $10'' \times 10''$ average maps were run at a correlation threshold of 0.8, but used an improved algorithm to minimize spurious detections, which is described in Appendix A.

3. A NEW DISTORTION MODEL FOR NIRC2'S NARROW CAMERA

Ground-based astrometric observations are subject to rapidly varying effects (such as instantaneous changes in the spatial pattern of PSF variation around the detector), which lead to measurable nonlinear residuals between positions even when comparing frames within a night (e.g., Lu 2008). In this work, we seek to characterize the static component of the distortion, which may be dominated by distortion within NIRC2 itself. Residuals between observed stellar positions in NIRC2 and their counterparts in a nominally distortion-free frame are represented as a single residual surface, which when smoothed, forms our

Table 2
Summary of GC Maser Mosaic Images

Date (UT)	Start Pos ^a (pixel)	$t_{\text{exp},i} \times \text{Co-add}$ (s)	N_{exp}^b	K'_{lim}^c (mag)	FWHM (mas)	Strehl	N_{stars}	σ_{pos} mas
2005 Jun 30	851, 426	0.181×60	2	15.6	62	0.25	1306	1.14
2006 May 3	852, 426	0.181×60	3	15.7	60	0.21	1372	1.13
2007 Aug 12	852, 425	0.181×60	3	15.7	58	0.23	1626	1.06
2008 May 15	856, 427	0.181×60	3	15.9	52	0.31	2017	1.04
2009 Jun 28	855, 426	0.181×60	9	16.2	63	0.20	2354	1.04
2010 May 4	858, 428	0.181×60	3	15.5	69	0.17	1174	1.08

Notes. All images taken at P.A. = 0° .

^a The X, Y position of IRS 16C in the first image of a given epoch.

^b The number of exposures per dither position.

^c K'_{lim} is the magnitude at which the cumulative distribution function of the observed K' magnitudes reaches 90% of the total sample size.

distortion model. The result is a model for the time-averaged distortion felt by the telescope and detector system.

3.1. Constructing the Model

To find the best-fit model for NIRC2's geometric optical distortion from the M92 observations, one must account for the fact that the ACS/WFC data do not suffer from DAR, while the NIRC2 data come from ground-based observations and therefore will be affected by the Earth's atmosphere (see Figure 4).

DAR will compress an image along the zenith direction, causing the apparent separation between a pair of stars to be smaller than their true separation. Since the stellar positions are first geometrically distorted by the atmosphere and then the telescope/instrument, it is best to “undo” these effects in the reverse direction. Assuming that one has a distortion solution for NIRC2 at hand, to convert observed positions to their counterparts in rectilinear space, the distortion solution should first be applied to the observed positions and then corrected for DAR. When attempting to *find* the distortion solution, however, the positions observed at NIRC2 cannot be corrected for DAR to compare with *HST* because we do not know the distortion-corrected positions this process require. Instead, DAR is applied to the *HST* positions to produce a set of reference positions that should correspond to distortion-free positions as observed through the atmosphere. Because the effects of DAR depend on the elevation and, to a much lesser extent, the atmospheric conditions of the observations, it is necessary to create a separate DAR-transformed ACS/WFC star list for each NIRC2 image and associated star list. To account for DAR, we follow the prescription for DAR given in Gubler & Tytler (1998). The stellar positions are only corrected for achromatic DAR, as the error from chromatic DAR is negligible (<0.2 mas) relative to the residual distortion in ACS/WFC (~ 0.5 mas). Neglecting chromatic effects, the DAR term (ΔR) depends on (1) the observed zenith angle of star 1, (2) the wavelength of the observations, (3) the observed zenith separation of star 1 and star 2, (4) the temperature at the observatory, (5) the pressure at the observatory, and (6) the relative humidity at the observatory. The atmospheric parameters of interest are downloaded from an archive maintained at the Canada–France–Hawaii Telescope (CFHT)⁸ for the night of each observation. These values are recorded every five minutes, allowing us to find the appropriate atmospheric conditions on Mauna Kea within three minutes of

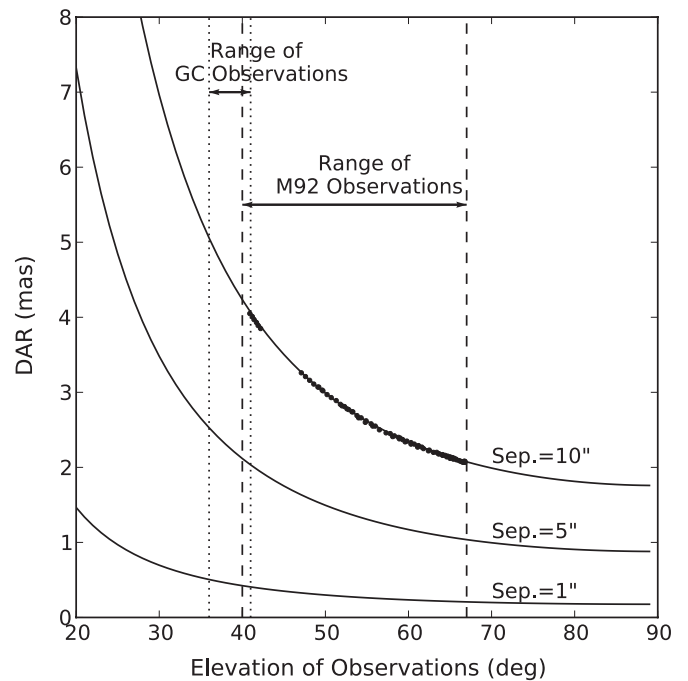


Figure 4. Predicted achromatic differential atmospheric refraction at a range of elevation angles for *typical* observing conditions at Keck. DAR causes the separation of two stars to appear smaller along the zenith direction and the change in the separation is shown for three pairs of stars separated by 1", 5", and 10". The black dots show the amount of DAR over the 10" field for each of the M92 observations used in the distortion solution. These are slightly offset from the predicted curve because the atmospheric conditions differed slightly from the reference conditions used to generate the curves. The range of our GC and M92 observations are also shown. In all of our analyses, we apply DAR corrections to each individual image based on the conditions at the time.

the observation (Lu 2008). As shown in Figure 4, the magnitude of the achromatic effect over the range of elevations for the M92 observations is expected to be ~ 2 – 4 mas across NIRC2's 10" field of view, along the elevation axis.

Each of the NIRC2 star lists described in Section 2.1 is then used as a reference coordinate system into which the ACS/WFC star list of positions is transformed. In this process, the ACS/WFC star list is transformed by minimizing the error-weighted (NIRC2 positional errors) net displacement for all the stars, allowing for translation, rotation, and a global plate scale (i.e., a four-parameter transformation model). This process is described in greater detail in Ghez et al. (2008) and Lu et al. (2009). Only sources that are cross identified in both the NIRC2

⁸ <http://kiloaoloa.soest.hawaii.edu/archive/wx/cfht/>

and ACS star lists are used in the remaining analysis. From the 79 separate alignments, a total of 2743 matches in stellar positions are obtained for a total of 150 independent stars. The differences in the matched positions, or deltas, are a result of the optical distortion in NIRC2.

The mapping of ACS positions to NIRC2 positions shows clear spatial structure across the detector, as expected from optical distortion (see Figure 5). However, some deltas are inconsistent with those in their immediate surroundings. These outliers are found by examining the vector deviations in 205×205 pixel bins and determining the average and standard deviation. Any 3σ outliers in either the X or Y direction are removed. A total of 75 deltas are removed based on this criterion. An additional cut ($>3\sigma$) in each of these bins is made on NIRC2 positional uncertainties, as they may vary with respect to detector position. This cut removes 73 data points, four of which were also eliminated by the first cut. These bins are examined a second time for vector outliers, as they often show a rather wide distribution. The average and standard deviation in each bin are recalculated and the vector outliers ($>3\sigma$) are removed once again. This resulted in an additional loss of 26 deltas.

Many of the eliminated measurements come from common stars or images. We therefore remove all measurements of the 9 out of 150 stars and of the 8 out of 79 images that were eliminated more than 20% of the time by the sigma-clipping process. Many of these problematic stars have close neighbors ($<0''.2$) that are not resolved or not well measured in the lower-resolution ACS observations (FWHM ~ 70 mas for the F814W observations). The majority of the rejected frames have exposure times less than 10 s, while the remaining frames are at least 30 s. This results in significantly higher centroiding uncertainties, residual atmospheric effects, and fewer stars detected. We note that our trimming criteria mentioned above also result in the exclusion of all data from the 2008 June epoch ($t_{\text{int}} = 9$ s), which coincidentally was the only M92 data set taken in LGS AO mode. Although the 2008 April data set had relatively long exposure times ($t_{\text{int}} = 48$ s), the observations were heavily impacted by clouds and the AO system was often unable to remain locked on the NGS. These rejected frames show a value of -1.0 in the last column of Table 1. Our final data set consists of 2398 positional deviations between ACS and NIRC2, with median centroiding uncertainty for the NIRC2 images of 0.035 pixel (~ 0.35 mas). The vector plot for this cleaned sample is shown in the bottom panel of Figure 5.

A bivariate B-spline is fit to the distortion map (Figure 5) using the SciPy package *interpolate*, and a look-up table sampled at each of the 1024×1024 NIRC2 pixels is subsequently produced. The effect of the smoothing factor (f ; which is related to the number of nearest-neighbor measurements used to calculate the smoothing) used in the interpolation routine was investigated extensively in order to find a good compromise between the closeness of fit and the smoothness of fit. The residuals between the original distortion vectors in the bottom panel of Figure 5 and the computed shift at the nearest pixel (from the smoothed look-up table) were measured. The median deviation is found to increase until $f \sim 150$, where it plateaus at a value of ~ 0.27 pixel. We choose for our interpolation the smoothing factor that gave nearly the lowest median deviation, $f = 135$. Although the deviations were lower for distortion solutions created with smaller smoothing factors, the edge effects were prominent in the look-up tables and the distribution of deviations was much larger (for details on surface fitting and the choice of smoothing factors, see Dierckx 1995). The resulting

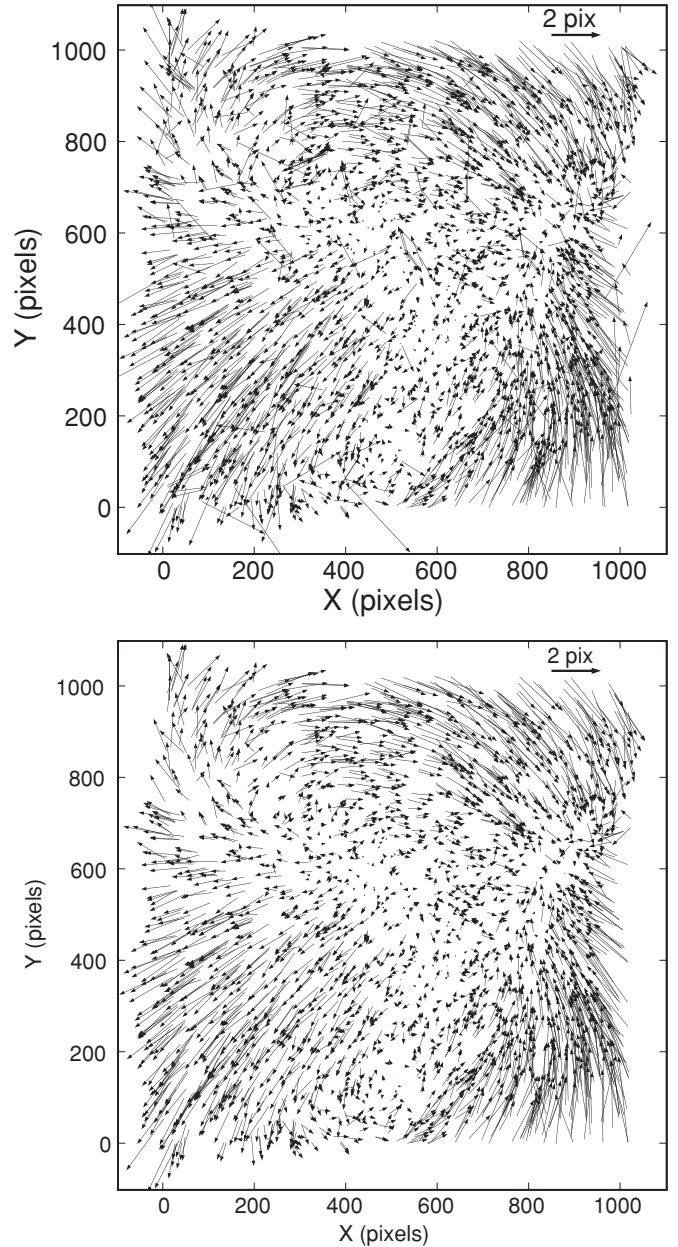


Figure 5. Optical distortion in the NIRC2 camera obtained from positional measurements of stars in the globular cluster M92. Arrows indicate the difference between measurements made with NIRC2 (arrow tail) and ACS/WFC (arrow head), which has a well-characterized distortion solution to the ~ 0.5 mas level (Anderson & King 2006; Anderson 2007). The two figures show pre- (top) and post- (bottom) trimming.

look-up tables for shifts in X and Y are shown in Figure 6 and are produced in the form of FITS files that may be fed into the IRAF routine, *Drizzle* (Fruchter & Hook 2002), to correct for the optical distortion. Figure 7 (left) shows a histogram of these values.

Statistical uncertainties in the distortion solution were computed by running a bootstrap analysis with 1000 trials. In each trial, we generated a random set of data pulled from the observed data, allowing for replacement after each data point was sampled, and then derived a distortion model from this resampled data set. The rms error with respect to the distortion solution (i.e., the actual distortion solution was taken as the average) was

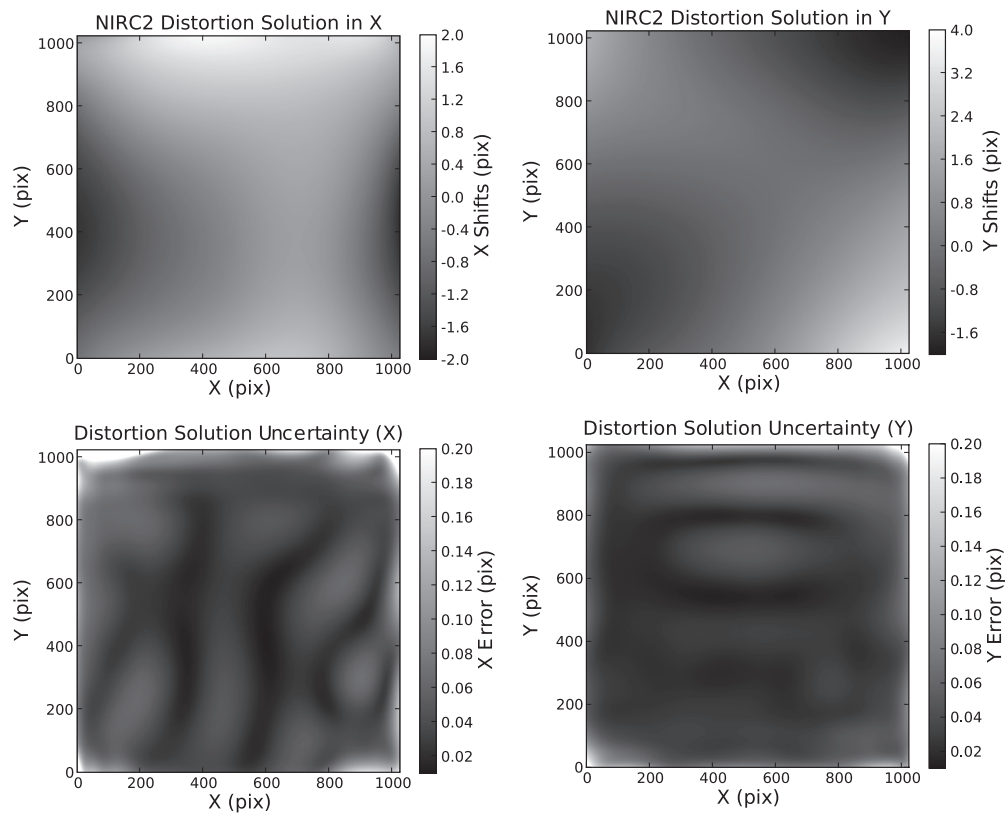


Figure 6. Top: distortion solution in the form of a look-up table for X (left) and Y (right). The tables give the X and Y values for each pixel required to remove the optical distortion from NIRC2 images. This was generated by fitting a surface to the distortion map in the bottom panel of Figure 5. Bottom: rms error of the 1000 simulations of the distortion solution based on M92 data (Section 3.1) for X (left) and Y (right). The images are shown in linear stretch. The average errors in X and Y are $(\sigma_X, \sigma_Y) = (0.05, 0.04)$ pixel $\sim (\sim 0.5, \sim 0.4)$ mas, respectively. Note that an additional error of 0.1 pixel is required to fully describe the uncertainty in the optical distortion (see Section 3.3).

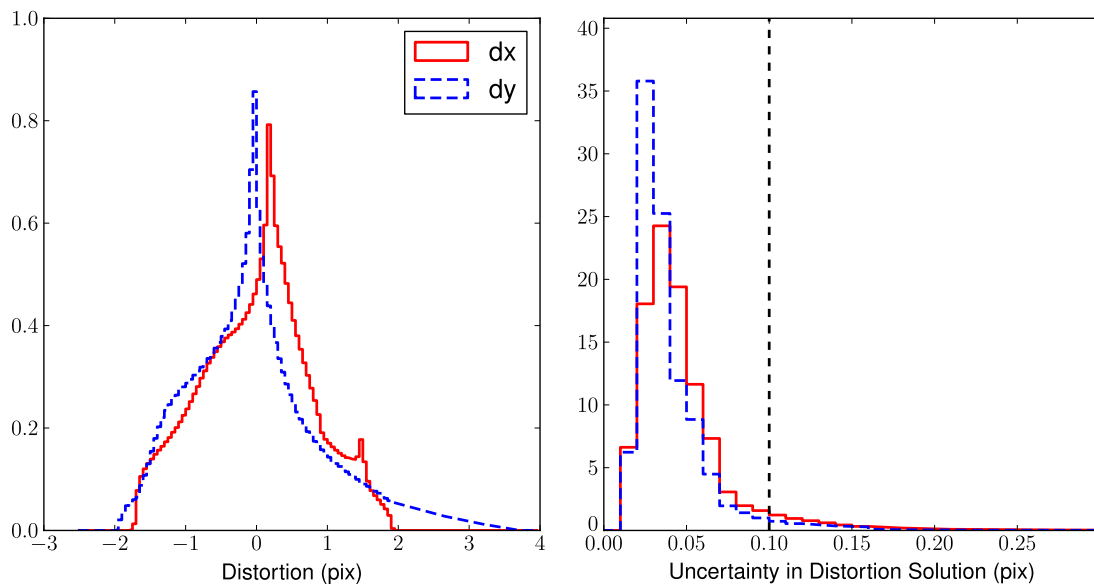


Figure 7. Left: distribution of the shifts in the distortion solution look-up table over all NIRC2 pixels for X (solid red) and Y (dashed blue). Right: distribution of the rms uncertainties from the 1000 simulations of the distortion solution. The average errors in X and Y are 0.05 ± 0.04 pixel and 0.04 ± 0.02 pixel, respectively. The vertical dashed line represents the additive error that is found when the models are tested with GC data (see Section 3.2).

(A color version of this figure is available in the online journal.)

calculated at each pixel and the results are shown in the bottom of Figure 6. The average errors in X and Y are $(\sigma_X, \sigma_Y) = (0.05, 0.04)$ pixel $\sim (0.5, 0.4)$ mas, respectively. We can see that the uncertainties are highest near the edge of the detector, where the spline algorithm is less robust. The uncertainties are also shown

in the form of a histogram in Figure 7 along with a histogram of the distortion solution itself.

To solve for the global plate scale and orientation that results from this new solution, we re-reduce the raw NIRC2 observations of M92 from all epochs and apply corrections for

distortion and DAR to these images. The distortion correction and DAR correction are applied to each image at the same time in the form of look-up tables using the *Drizzle* algorithm as implemented in IRAF (Fruchter & Hook 2002). The look-up tables are specified in *Drizzle* using the *xgeom* and *ygeom* keywords and are FITS files of the same dimensions as the science image. Because DAR depends on the zenith angle and atmospheric conditions, both of which vary in time, the look-up tables are created by first including the distortion solution and then applying the necessary DAR correction. Two FITS files, one for shifts in X and one for shifts in Y , are created for each NIRC2 observation and contain the shifts to be applied to each pixel in the image. From these distortion- and DAR-corrected NIRC2 images, star lists were generated and aligned with the original ACS star list (without DAR) as described above. The weighted average of the plate scale is $\langle s \rangle = 9.950 \pm 0.003_{\text{stat}} \pm 0.001_{\text{abs}}$ mas pixel $^{-1}$. The difference between the orientation given in the header of the NIRC2 images⁹ and the measured orientation is on average (weighted) $0:254 \pm 0:014_{\text{stat}} \pm 0:002_{\text{abs}}$. We use the rms errors of the average values from each epoch as the statistical uncertainties, and the absolute errors are the rms errors in the ACS/WFC plate scale and orientation angle (van der Marel et al. 2007). The results from each epoch of M92 data are shown in Table 4.

The new distortion solution and its errors are made public and may be obtained in the form of FITS files.¹⁰

3.2. Testing the Model

There are two parts to the error in the distortion model when applied to a real data set: static distortion error (hereafter “residual distortion,” discussed here) and time-varying effective distortion (discussed in Section 3.3). The residual distortion map on the detector is unknown, but is likely to be highly spatially correlated. The spurious position shift due to residual distortion when comparing two measurements is a function both of the size of the residual distortion itself, and the difference ΔR in location on the detector between the two measurements.

To estimate the size of the residual distortion from our model, we consider two cases. In the first, sets of images are taken at two very different P.A.s so that the distance ΔR between two measurements of the same object (and therefore the degree to which the residual distortion varies between measurements) is a strong function of position on the detector. In the second, images are taken at the same P.A. so that ΔR is constant over the image, but are widely dithered (60% of the detector side-length) so that the residual distortion is sampled at widely separated detector locations for all objects.

In both cases, we compare our new distortion model with two previous solutions, which we refer to as the “pre-ship” and the “P. Brian Cameron (PBC)” solutions. The pre-ship solution,¹¹ which is known to ~ 4 mas, was found using a pinhole mask and is in the form of a third-order polynomial. The more recent solution by P. B. Cameron, also from a pinhole mask, is a fourth-order polynomial and improves upon the former solution mainly along the X axis.¹²

First, we use the two high precision data sets taken of the central $10'' \times 10''$ on 2007 May 17 and May 20 at two different P.A.s (0° and 200°) with roughly the same central position (Section 2.2). The typical NIRC2 positional uncertainties (the standard deviation, δ_{pos}) for the P.A. = 0° and P.A. = 200° images are ~ 0.013 pixel and ~ 0.018 pixel, respectively. The P.A. = 200° image was transformed into the P.A. = 0° image’s coordinate system, again allowing for translation, rotation, and global plate scale. The differences in the aligned positions of stars with $K < 14.5$ are shown in Figure 8. This analysis gives an average residual distortion by comparing the positions of a star at two distinct locations on the detector. Our new solution shows significantly less residual structure than the previous solutions. To estimate the magnitude of the residual distortion (σ), we compute the rms error of the offsets (Δ) between the positions in the two images in the X and Y directions separately¹³ and correct for the positional measurement error from both images (δ):

$$\sigma_x = \sqrt{\frac{1}{2} \sum_i^{N_{\text{stars}}} \frac{(\Delta_{x,i} - \langle \Delta_x \rangle)^2}{(N_{\text{stars}} - 1)} - \frac{1}{2} (\delta_{\text{pos},0^\circ}^2 + \delta_{\text{pos},200^\circ}^2)}, \quad (1)$$

where N_{stars} is the number of stars matched across the two images, and $\delta_{\text{pos},0^\circ}$ and $\delta_{\text{pos},200^\circ}$ are the positional uncertainties (quoted above) for stars brighter than $K = 14.5$ in the P.A. = 0° and P.A. = 200° images, respectively. Average positional uncertainties are subtracted, as opposed to each star’s individual uncertainty since most stars brighter than $K = 14.5$ have similar centroiding uncertainties. We compute σ_y similarly. We note that the division by 2 is necessary to determine the residual distortion incurred *per* NIRC2 image. This results in estimates of the residual distortion of $(\sigma_{x,0}, \sigma_{y,0}) = (0.12, 0.11)$ pixel, $(0.17, 0.28)$ pixel, and $(0.27, 0.22)$ pixel for the new, PBC, and pre-ship solutions, respectively. Thus, the new solution results in smaller residuals by a factor of ~ 2 – 2.5 over both of the previous solutions. The uncertainty in the distortion models has not been removed from these values, as the uncertainty in the PBC and pre-ship solutions is unknown. We can, however, remove the average uncertainty in our new model in quadrature (Figure 6, bottom) to obtain a final measure of the residual distortion: $(\sigma_{x,0}, \sigma_{y,0}) = (0.11, 0.10)$ pixel.

As an additional check on the distortion solution, we use the images from widely dithered ($6''$) 2008 May data set taken at P.A. = 0° (Section 2.2), which, unlike the test just described, maintain the independence of the X and Y axes as they are shifted relative to one another by only a translation. Largely dithered data sets are essential in testing the distortion solution because stars are placed on very different locations on the detector and therefore provide a sensitive test of residual distortion. These data have an average rms error on the positions of 0.05 pixel. Only four overlapping fields, each of which was imaged three times and whose centers are the corners of a $6'' \times 6''$ box, were examined from this data set (Figure 9). Only stars detected in at least 6 of the 12 images (and therefore at least two of the four overlapping fields) were kept in the analysis. The stars had to also be detected in all three exposures at each dither position, and the average of the positions in these three exposures was taken as the position at the corresponding dither position. The error $(\sigma_{x,i}, \sigma_{y,i})$ from residual optical distortion of each star’s offsets (Δ_x, Δ_y) from IRS 16SW-E (which was in each of the

⁹ The NIRC2 FITS header keyword for the P.A., ROTPOSN, includes a +0:7 offset (given by header keyword INSTANGL), the observatory value for the angle offset of NIRC2. The nominal P.A. for NIRC2 in our analysis is taken as (ROTPOSN-INSTANGL).

¹⁰ <http://www.astro.ucla.edu/~ghezgroup/distortion>

¹¹ http://www2.keck.hawaii.edu/inst/nirc2/preship_testing.pdf

¹² <http://www.astro.caltech.edu/~pbc/AO/distortion.pdf>

¹³ These residuals are measured in the P.A. = 0° image’s coordinate system, as this was the reference onto which the P.A. = 200° image was transformed.

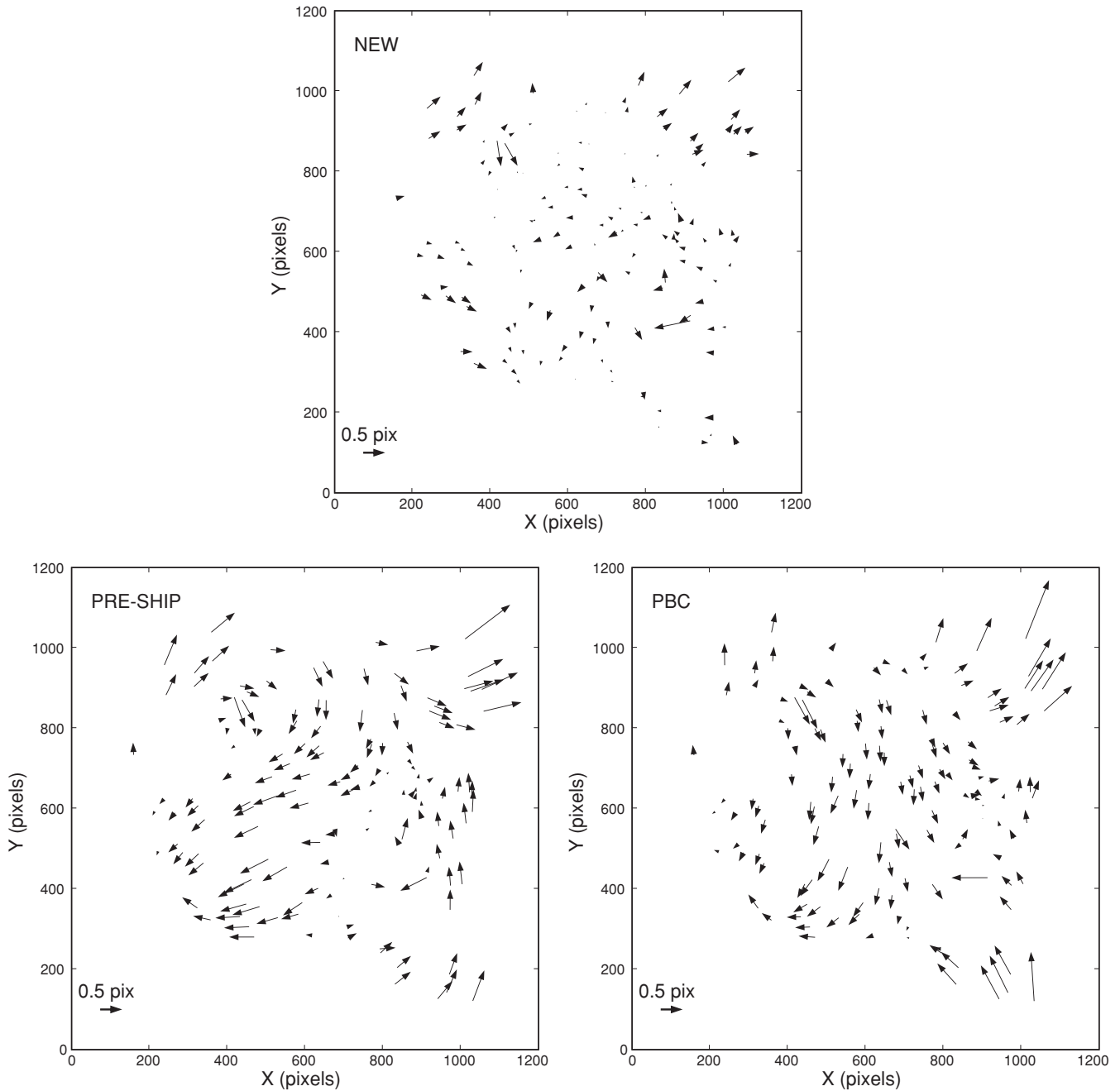


Figure 8. Differences between stellar positions in GC images taken at P.A. = 200° (arrow tail) and P.A. = 0° (arrow head) after applying the new (top), pre-ship (bottom left), and PBC (bottom right) distortion solutions. While some residual distortion remains, much of the structure seen after using the pre-ship solution is removed with the new solution. The residual distortion remaining is $(\sigma_{x,0}, \sigma_{y,0}) = (0.12, 0.11)$ pixel, $(0.17, 0.28)$ pixel, and $(0.27, 0.22)$ pixel for the new, PBC, and pre-ship solutions, respectively.

four fields) was computed as

$$\sigma_{x,i} = \sqrt{\frac{1}{2} \sum_j^{N_{\text{fields}}} \frac{(\Delta x_j - \langle \Delta x_j \rangle)^2}{N_{\text{fields}} - 1} - \frac{1}{2} \frac{1}{N_{\text{fields}}} \sum_j^{N_{\text{fields}}} \left(\frac{\delta_{\text{pos,IRS 16SW-E}}^2}{N_{\text{exp}} - 1} + \frac{\delta_{\text{pos},i}^2}{N_{\text{exp}} - 1} \right)} \quad (2)$$

and likewise for $\sigma_{y,i}$, where we divide by the number of overlapping fields in which a star was detected (N_{fields}), and we correct for the NIRC2 positional measurement error (the standard deviation, δ_{pos}) per exposure (N_{exp}) for both IRS

16SW-E and star i . The factor of 2 in the denominator accounts for the fact that the distortion affects both stars, IRS 16SW-E and star i . These errors from the residual optical distortion are shown in Figure 10 for all three solutions. The median values (σ_x, σ_y) are $(0.05, 0.06)$ pixel, $(0.07, 0.15)$ pixel, and $(0.18, 0.17)$ pixel, for the new, PBC, and pre-ship solutions, respectively. The new solution was found to significantly improve positional measurements overall as compared to both of the previous solutions and in particular, it is a factor of 3 better in the Y direction over the more recent PBC solution. As mentioned above, the uncertainties in the distortion models have not been removed from these values, as they are unknown for the two previous solutions. For the new distortion solution, however,

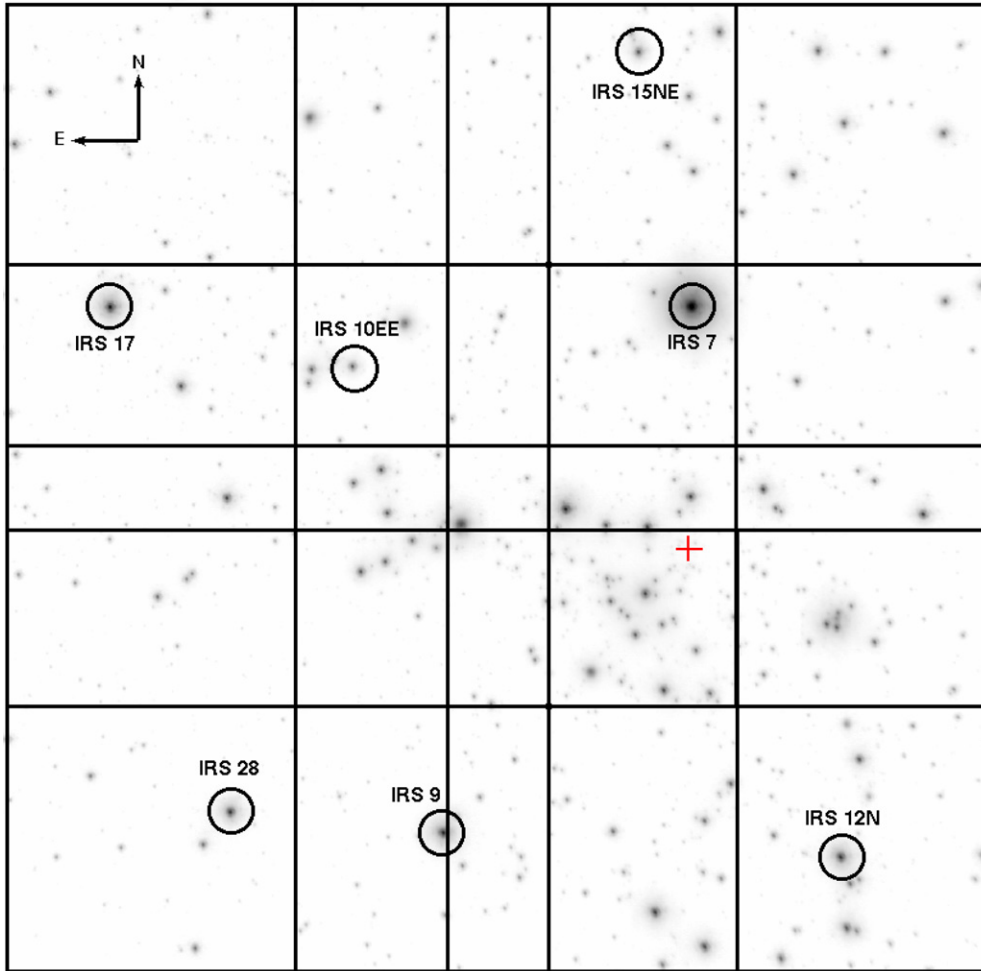


Figure 9. NIRC2 K' mosaic image of the GC scaled to show the bright stars. The full field is $22'' \times 22''$. The black boxes show the nine dither positions making up the mosaic, with each box corresponding to the $10'' \times 10''$ NIRC2 field of view. The seven SiO masers used in the construction of the Sgr A*-radio reference frame are circled, and Sgr A* is marked with a red cross. The four images that make up the southwest corner of the mosaic were used in Section 3.2 to determine the quality of the distortion solution.

(A color version of this figure is available in the online journal.)

the rms offsets are consistent with the average uncertainty in the distortion model itself.

The errors computed using the pairwise analysis are approximately half the size of those reported using the GC observations at two P.A.s. We note that the pairwise analysis uses measurements that have uncertainties that are a factor of 3 larger than our other test and is therefore more sensitive to the removal of the measurement bias term. We take as the final residual error term for the new NIRC2 distortion solution the value from the first test: $(\sigma_{x,0}, \sigma_{y,0}) = (0.11, 0.10)$ pixel.

3.3. Additional Sources of Uncertainty

While the new distortion solution represents a significant step forward in our astrometric capabilities, it still leaves ~ 0.1 pixel or ~ 1 mas residual distortion in LGS AO images that are widely dithered or taken at different P.A.s. The residual distortion is twice as large as the estimated uncertainties in the distortion solution (~ 0.05 pixel; Figure 7) and must come from sources of uncertainty that are not accounted for in our analysis. Below we consider two possibilities, time-variable distortion, and the difference between NGS AO and LGS AO observations.

To test the stability of the camera's distortion, we created a distortion solution with data points from 2007, the year with

the most data ($N = 1711$). A smoothing factor of $f = 120$ was used for the spline fitting and was determined in the same manner as our new distortion solution. As the number of data points from each of the years 2008 ($N = 253$) and 2009 ($N = 489$) was not sufficient to make separate distortion solutions for these years, we take the differences between the 2007-only distortion solution and the actual measured data from each of the individual years (see Table 1). We find no significant differences (0.05 ± 0.30 pixel and 0.09 ± 0.29 pixel for 2008 and 2009, respectively), suggesting that the distortion solution is stable within our measurement uncertainties. As a check, comparing the data from 2007 to the 2007-only solution gives an average difference of 0.01 ± 0.22 pixel, which has a smaller rms error since it was the data set used to create the single-year model. Based on this analysis, we conclude that there is no evidence for time-dependent changes.

While we tested our distortion solution on LGS AO data, the model itself was computed using only NGS data, as the six LGS frames from 2008 June were thrown out based on the cuts mentioned in Section 3.1. To test the possibility that the NGS and LGS AO systems have different distortion solutions, we compare GC data taken in both LGS and NGS modes, but otherwise the same setup and in the same night in 2008 May. The data were reduced using the usual data reduction steps (see

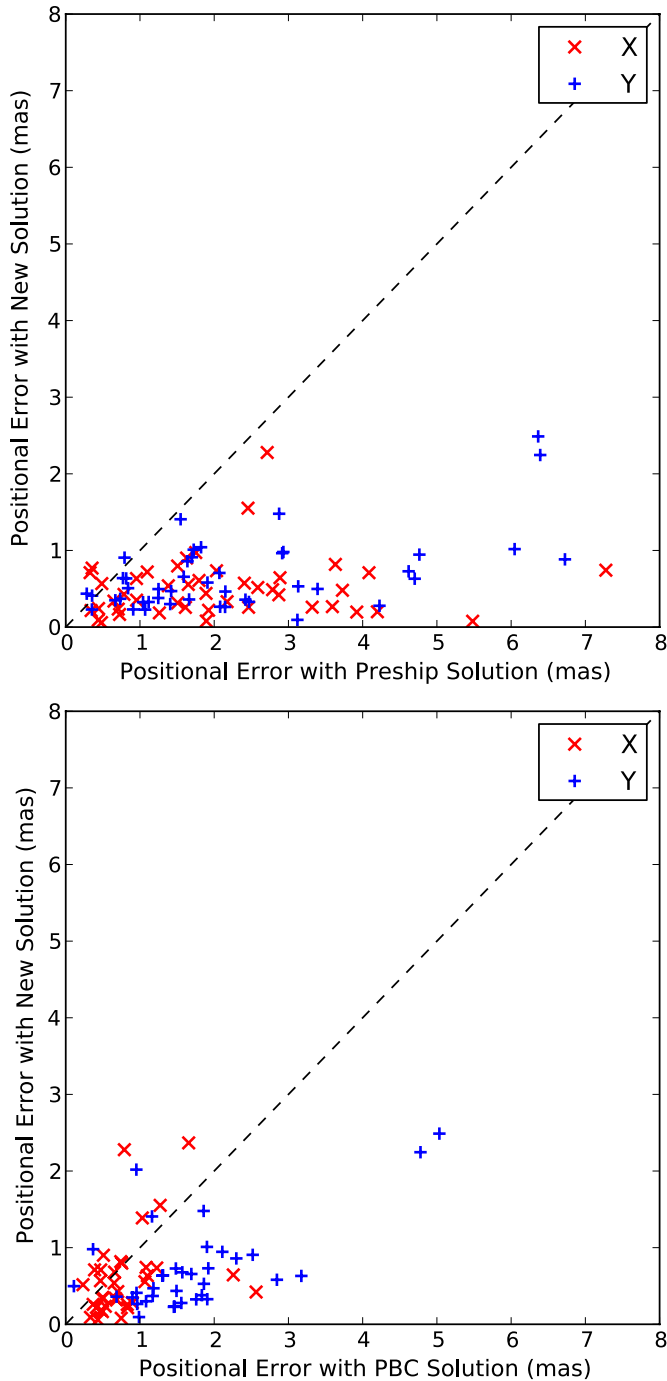


Figure 10. Pairwise analysis on widely dithered GC data taken in 2008 May. The rms error of the positional offsets from IRS 16SW-E are plotted. The plots compare the rms error values from images corrected with the new vs. the pre-ship distortion solution (top) and the new vs. the PBC distortion solution (bottom). The new solution is a factor of ~ 3 – 4 improved in both X (red crosses) and Y (blue plus signs) over the pre-ship solution and in Y over the PBC solution. (A color version of this figure is available in the online journal.)

Ghez et al. 2008), and final LGS- and NGS-only images of the GC were produced. The astrometric precision for each of these images was 0.007 pixel (NGS) and 0.012 pixel (LGS) for stars with $K < 15$. The NGS image was transformed into the LGS image’s coordinate system allowing only for translation between the two frames. Differences between the transformed positions would indicate a possible difference in the distortion between the LGS and NGS observing modes. The rms difference in the aligned positions, corrected for measurement error bias, is only

$(\Delta_x, \Delta_y) = (0.06, 0.05)$ pixel (1σ) and is therefore comparable to the error in the distortion model (~ 0.05 pixel, Figure 7). Thus, given the uncertainties in the distortion solution, we do not see a difference in the astrometry from images taken in NGS or LGS mode and conclude that this is a negligible contribution to the residual distortion.

While we have not identified the source of residual distortion, we can functionally include it by adding a constant term of 0.1 pixel (1 mas) in quadrature with the error map of the distortion (see Section 3.1) when analyzing astrometric data. We note that while these error terms are important for our localization of Sgr A*-radio in our infrared reference frame (Section 4.1), they do not come into consideration for relative proper motion measurements based on data using similar observational setups.

4. APPLICATION TO THE GALACTIC CENTER

Here we apply the new geometric optical distortion model and DAR corrections from Section 3.1 to Keck/NIRC2 observations of the GC in order to construct a new IR reference frame (Section 4.1) that is significantly more accurate and stable than those that have been made in the past (Section 4.2). We also measure the motion of the nuclear cluster in this well-defined reference frame and generate a set of secondary infrared astrometric standards that are helpful for doing astrometry over much smaller fields of view (Section 4.3).

4.1. Construction of an Infrared, Sgr A*-Radio Rest Frame

Measurements of seven SiO masers that are detectable in the radio and infrared wavelengths are used to transform the IR maser mosaics into an Sgr A*-radio rest frame. At radio wavelengths, each of these masers has well-measured positions and velocities with respect to Sgr A* (see, e.g., Reid et al. 2003, 2007). In this analysis, we use radio positions and proper motions from M. Reid (2010, private communication), who has improved the values compared to what is published in Reid et al. (2007) by adding one more epoch of observations and by applying a correction for the effects of differential nutation. The radio maser positions were propagated using the radio proper motion measurements to create a star list at the epoch of each IR mosaic. Each of the six infrared mosaics was aligned with a four-parameter model (two-dimensional translation, rotation, and a single pixel scale) to the radio maser star list by minimizing the error-weighted net displacements, D , for the masers, where the infrared positional errors include the positional rms errors (from the three subset images; see Section 2.2), as well as errors from the distortion model (see Appendix B). The net displacement and the weighting scheme used are described in Appendix A of Ghez et al. (2008). Errors in the transformation to the Sgr A*-radio rest frame in each epoch were determined using a jack-knife sampling technique, in which one maser at a time is excluded from the alignment. The various sources of error in our astrometry are broken down in Table 3. Distortion errors generally dominate the individual IR positional uncertainties of these masers, with the exception of IRS 12N and IRS 28, each of which is in only one pointing and is furthest from the tip-tilt star, where the AO corrections are the poorest. All the transformed IR positions agree with the radio positions to within $\sim 1\sigma$ of each other, suggesting that our uncertainties are well characterized and that we are not missing large systematic error sources.

The NIRC2 pixel scale and orientation values obtained from the SiO maser alignment are similar to those obtained from the M92 study (Table 4). We note, however, that the rms scatter

Table 3
Measurements of SiO Masers

Star Name	(IR–Radio) Position			Uncertainty in Radio		Uncertainty in IR Centroid		Uncertainty in Alignment		Distortion Error ^a		σ Offset		DAR ^b
	X (mas)	Y (mas)	Total (mas)	X (mas)	Y (mas)	X (mas)	Y (mas)	X (mas)	Y (mas)	X (mas)	Y (mas)	X (mas)	Y (mas)	
IRS 9 (Avg)	-1.44	0.31	1.65	0.40	0.67	0.91	1.19	0.78	0.55	1.04	1.05	-0.82	0.13	-2.32
2005 Jun	-1.54	0.90	1.78	0.30	0.50	0.36	0.62	0.40	0.60	1.04	1.05	-1.27	0.62	-2.95
2006 May	-2.94	1.31	3.22	0.30	0.50	2.94	3.02	1.30	0.60	1.04	1.06	-0.87	0.40	-2.01
2007 Aug	-1.00	0.17	1.01	0.40	0.60	0.59	1.01	0.50	0.30	1.04	1.05	-0.74	0.11	-1.77
2008 May	-1.60	-0.43	1.66	0.40	0.70	0.48	0.62	0.80	0.70	1.05	1.05	-1.10	-0.27	-1.79
2009 Jun	-0.99	-0.84	1.30	0.50	0.80	0.86	0.89	0.90	0.50	1.05	1.05	-0.58	-0.50	-2.84
2010 May	-0.54	0.73	0.91	0.50	0.90	0.25	1.00	0.80	0.60	1.05	1.05	-0.38	0.40	-2.54
IRS 7 (Avg)	1.26	-6.61	6.75	5.02	5.03	0.32	0.40	0.28	1.32	1.09	1.07	0.24	-1.24	2.24
2005 Jun	1.96	-5.27	5.62	5.00	5.00	0.20	0.68	0.40	0.80	1.09	1.07	0.38	-1.01	2.21
2006 May	1.17	-6.85	6.95	5.00	5.00	0.51	0.31	0.30	1.50	1.09	1.07	0.23	-1.28	2.25
2007 Aug	1.57	-6.35	6.54	5.00	5.00	0.35	0.19	0.30	1.10	1.09	1.07	0.31	-1.21	2.29
2008 May	0.79	-7.89	7.93	5.00	5.00	0.28	0.27	0.20	1.50	1.09	1.07	0.15	-1.48	2.30
2009 Jun	1.47	-7.08	7.23	5.00	5.10	0.35	0.38	0.30	1.60	1.09	1.07	0.29	-1.30	2.17
2010 May	0.59	-6.22	6.25	5.10	5.10	0.22	0.56	0.20	1.40	1.08	1.07	0.11	-1.15	2.20
IRS 12N (Avg)	-3.46	-3.46	5.17	0.47	0.50	3.35	5.29	1.32	0.95	1.03	1.02	-1.08	-0.87	-2.94
2005 Jun	-1.81	-5.37	5.67	0.40	0.40	0.72	1.26	0.70	0.80	1.03	1.03	-1.21	-2.89	-2.53
2006 May	-4.64	-1.39	4.84	0.40	0.40	3.81	1.88	2.00	1.10	1.04	1.04	-1.04	-0.57	-3.13
2007 Aug	-1.30	-0.47	1.38	0.40	0.50	0.30	2.53	0.90	0.60	1.03	1.02	-0.89	-0.17	-3.35
2008 May	-3.35	-5.81	6.71	0.50	0.50	1.82	7.26	1.40	1.20	1.02	1.01	-1.31	-0.78	-3.36
2009 Jun	-3.99	-3.65	5.41	0.50	0.60	10.51	10.45	1.50	1.00	1.02	1.02	-0.37	-0.35	-2.54
2010 May	-5.70	-4.07	7.00	0.60	0.60	2.95	8.36	1.40	1.00	1.04	1.00	-1.64	-0.48	-2.74
IRS 28 (Avg)	-2.03	6.53	7.23	0.72	0.63	2.11	5.56	0.60	0.62	1.05	1.04	-0.84	1.34	-1.91
2005 Jun	-3.88	5.57	6.79	0.80	0.70	2.18	0.59	0.50	0.60	1.05	1.04	-1.49	3.69	-3.09
2006 May	-0.66	2.32	2.41	0.70	0.60	1.79	6.35	0.90	0.90	1.06	1.01	-0.28	0.36	-1.33
2007 Aug	-1.04	-0.54	1.17	0.60	0.50	2.49	1.77	0.30	0.40	1.07	1.03	-0.37	-0.25	-0.84
2008 May	-2.22	5.73	6.15	0.60	0.50	1.17	2.10	0.60	0.70	1.06	1.03	-1.24	2.30	-0.87
2009 Jun	-1.71	1.99	2.62	0.70	0.70	0.61	2.34	0.60	0.50	1.05	1.04	-1.12	0.74	-2.93
2010 May	-2.66	24.09	24.24	0.90	0.80	4.45	20.22	0.70	0.60	1.04	1.10	-0.57	1.19	-2.37
IRS 10EE (Avg)	0.71	1.75	2.00	0.32	0.38	0.39	0.45	0.40	0.73	1.11	1.03	0.57	1.24	2.03
2005 Jun	0.75	1.00	1.25	0.20	0.30	0.13	0.90	0.50	0.50	1.11	1.03	0.61	0.67	1.12
2006 May	-0.17	2.63	2.64	0.30	0.30	0.99	0.29	0.30	0.70	1.11	1.04	-0.11	2.00	2.46
2007 Aug	0.12	1.94	1.94	0.30	0.40	0.43	0.32	0.40	0.70	1.10	1.04	0.09	1.44	2.89
2008 May	1.19	1.01	1.56	0.30	0.40	0.31	0.14	0.50	0.80	1.10	1.04	0.93	0.73	2.88
2009 Jun	1.13	1.72	2.06	0.40	0.40	0.33	0.44	0.40	0.80	1.11	1.04	0.88	1.20	1.20
2010 May	1.27	2.18	2.52	0.40	0.50	0.19	0.60	0.30	0.90	1.11	1.03	1.03	1.38	1.64
IRS 15NE (Avg)	1.93	4.55	5.06	0.40	0.50	0.50	0.68	0.52	1.58	1.12	1.11	1.40	2.10	4.62
2005 Jun	2.89	3.25	4.35	0.30	0.40	0.41	0.34	0.60	1.00	1.11	1.11	2.12	2.05	4.42
2006 May	2.41	2.69	3.61	0.30	0.40	0.09	0.62	0.60	1.80	1.12	1.11	1.84	1.20	4.70
2007 Aug	1.95	4.11	4.55	0.40	0.50	0.49	0.73	0.50	1.30	1.11	1.12	1.42	2.13	4.85
2008 May	1.80	5.32	5.62	0.40	0.50	0.10	0.23	0.50	1.80	1.11	1.11	1.40	2.43	4.86
2009 Jun	1.63	5.66	5.89	0.50	0.60	0.61	0.72	0.50	1.90	1.12	1.11	1.12	2.37	4.37
2010 May	0.91	6.27	6.34	0.50	0.60	1.28	1.44	0.40	1.70	1.12	1.11	0.50	2.45	4.48
IRS 17 (Avg)	-0.85	0.34	1.54	4.52	2.35	0.51	0.46	0.83	0.53	1.12	1.04	-0.17	0.21	2.82
2005 Jun	-0.12	0.97	0.98	3.20	1.60	0.39	0.05	0.80	0.40	1.13	1.04	-0.03	0.50	1.27
2006 May	-0.48	1.57	1.64	3.50	1.80	1.00	0.45	0.80	0.60	1.12	1.04	-0.12	0.71	3.55
2007 Aug	-1.55	1.37	2.07	4.10	2.10	0.70	0.58	0.70	0.50	1.13	1.05	-0.36	0.56	4.28
2008 May	-0.35	0.00	0.35	4.60	2.40	0.18	0.28	1.00	0.50	1.12	1.04	-0.07	0.00	4.26
2009 Jun	-1.77	0.35	1.80	5.50	2.90	0.16	0.38	0.90	0.50	1.12	1.04	-0.31	0.11	1.41
2010 May	-0.86	-2.23	2.39	6.20	3.30	0.63	1.01	0.80	0.70	1.12	1.04	-0.13	-0.61	2.16

Notes.^a Distortion error includes the residual distortion term described in the text.^b DAR relative to the center of the image.

shows a larger variation between the epochs than the uncertainty inferred from the jack-knife analysis of each epoch. We therefore take the rms values as our estimates of the uncertainties for our average pixel scale and orientation angle given in Table 4. The weighted average NIRC2 plate scale and angle offset from the

IR to radio alignments are 9.953 ± 0.002 mas pixel⁻¹ and $0^{\circ}249 \pm 0^{\circ}012$, respectively. We average the results from the two methods (SiO masers and M92) to obtain our final values for the NIRC2 pixel scale and orientation angle, 9.952 ± 0.002 mas pixel⁻¹ and $0^{\circ}252 \pm 0^{\circ}009$, respectively. Thus, $0^{\circ}252$ must be

Table 4
NIRC2 Plate Scale and Orientation

Method	Plate Scale (mas pixel ⁻¹)	Orientation (deg)
Calibrated w.r.t. ACS observations of M92 ^a	9.950 ± 0.003 ± 0.001	0.254 ± 0.014 ± 0.002
2007 Jun	9.948 ± 0.001 ± 0.001	0.249 ± 0.006 ± 0.002
2007 Jul	9.948 ± 0.001 ± 0.001	0.256 ± 0.006 ± 0.002
2008 Apr	9.946 ± 0.007 ± 0.001	0.276 ± 0.030 ± 0.002
2008 Jun	9.952 ± 0.003 ± 0.001	0.270 ± 0.009 ± 0.002
2008 Jul	9.951 ± 0.002 ± 0.001	0.248 ± 0.004 ± 0.002
2009 May	9.949 ± 0.002 ± 0.001	0.282 ± 0.013 ± 0.002
Calibrated w.r.t. VLA observations of GC masers ^a	9.953 ± 0.002	0.249 ± 0.012
2005 Jun	9.952 ± 0.001	0.237 ± 0.003
2006 May	9.955 ± 0.001	0.248 ± 0.007
2007 Aug	9.950 ± 0.001	0.253 ± 0.003
2008 May	9.954 ± 0.001	0.271 ± 0.005
2009 Jun	9.952 ± 0.001	0.253 ± 0.005
2010 May	9.955 ± 0.001	0.253 ± 0.005
Final value ^b	9.952 ± 0.002	0.252 ± 0.009

Notes. Statistical (first) and absolute (second) uncertainties are shown for the ACS observations (see Section 2.1).

^a Weighted averages are taken for the final values for each method. We use the more conservative rms errors as the uncertainties on these values.

^b Average of each method's weighted average (see Note "a").

Table 5
Astrometry of SiO Masers

Maser	K (mag)	$\bar{\chi}^2$ ^a	IR T_0 (year)	IR + Radio T_0 ^b (year)	(IR–Radio) X Position ^c (mas)	(IR–Radio) Y Position ^c (mas)	(IR–Radio) X Velocity (mas yr ⁻¹)	(IR–Radio) Y Velocity (mas yr ⁻¹)
IRS 9	9.063	0.29	2007.7	2007.2	-1.32 ± 1.11 ± 0.34	0.35 ± 1.17 ± 0.57	0.18 ± 0.18 ± 0.08	-0.23 ± 0.26 ± 0.14
IRS 7	7.658	0.68	2007.7	2007.2	1.46 ± 1.11 ± 5.00	-6.24 ± 1.22 ± 5.00	-0.25 ± 0.09 ± 0.22	-0.28 ± 0.31 ± 0.30
IRS 12N	9.538	0.60	2006.4	2006.4	-1.88 ± 1.26 ± 0.42	-2.74 ± 1.59 ± 0.47	-0.28 ± 0.49 ± 0.05	1.24 ± 1.03 ± 0.06
IRS 28	9.328	1.19	2007.6	2007.6	-2.12 ± 1.34 ± 0.62	3.93 ± 1.41 ± 0.52	0.16 ± 0.47 ± 0.22	-0.95 ± 0.49 ± 0.24
IRS 10EE	11.270	0.64	2008.1	2007.7	0.62 ± 1.14 ± 0.29	1.75 ± 1.13 ± 0.32	0.17 ± 0.12 ± 0.04	-0.01 ± 0.24 ± 0.05
IRS 15NE	10.198	0.06	2007.4	2007.1	2.31 ± 1.16 ± 0.36	3.90 ± 1.31 ± 0.47	-0.33 ± 0.20 ± 0.05	0.68 ± 0.39 ± 0.06
IRS 17	8.910	0.90	2007.7	2005.1	-0.68 ± 1.22 ± 3.72	0.80 ± 1.08 ± 1.91	-0.23 ± 0.24 ± 0.99	-0.33 ± 0.15 ± 0.54
Weighted average ^d		0.62		2006.9	-0.31 ± 0.55	1.44 ± 0.59	0.02 ± 0.09	-0.06 ± 0.14

Notes. Infrared (first) and radio (second) formal uncertainties are reported for each maser's position and velocity. Average distortion errors ($\sigma \sim 1$ mas) for each maser are added in quadrature to the infrared formal uncertainties. X and Y increase to the east and north, respectively.

^a $\bar{\chi}^2$ is the average of the X and Y χ^2 per degree of freedom.

^b Average T_0 from both IR and radio measurements weighted by velocity errors (see Equation (3)).

^c Positional offsets computed for the common epoch of 2006.9.

^d Weighted average and error in the weighted average are reported for all columns except the $\bar{\chi}^2$ and T_0 columns, where we report the average.

added to the presumed P.A. (ROTPOSN–INSTANGL) in order to get the true P.A. of an NIRC2 image (i.e., the NIRC2 columns must be rotated eastward of north by 0:252).

Our transformed IR positions from the mosaic images provide a calibrated astrometric reference frame in which Sgr A* is at rest at the origin. Comparison of the SiO masers as measured in the IR and radio provide estimates of how well we can localize the position and velocity of Sgr A*-radio within this reference frame. For each maser, a linear motion model is obtained by fitting a line to the star's transformed infrared positions as a function of time. In this initial step, the positional uncertainties include only the centroiding and alignment errors; the distortion uncertainty (see Appendix B) is omitted here, since it is correlated across all epochs. Furthermore, the model fit is calculated with respect to $T_{0,IR}$, which is the average time of the IR positional measurements, weighted by the average of the X and Y positional uncertainties. Figures 11 and 12 show the resulting fits, which have an average reduced χ^2 value of 0.62 (see Table 5), and the uncertainties in the resulting

fit parameters were determined from the covariance matrix. In these figures, and in all other cases, X and Y increase to the east and north, respectively. While the reduced χ^2 values suggest that the uncertainties may be overestimated (possibly due to IRS 7; see Appendix C), we err on the conservative side and do not re-scale our positional measurements. The velocities measured in the infrared are statistically consistent with the radio proper motion values.¹⁴ Based on the weighted average of the velocity differences between the infrared and radio reference frames, we conclude that Sgr A* is at rest to within ~ 0.09 mas yr⁻¹ (compared to ~ 0.03 mas yr⁻¹ in the radio reference frame).

While increasing the time baseline and depth of the infrared measurements will improve upon this precision, we note that 4 out of 14 one-dimensional relative velocity measurements are already limited by the radio measurements. Further improvements in the radio will ultimately be required to create a

¹⁴ We note that using the latest radio values reduces the uncertainty in tying the IR and radio measurements, reported in Table 5, by 40% compared to the same analysis carried out using the radio values from Reid et al. (2007).

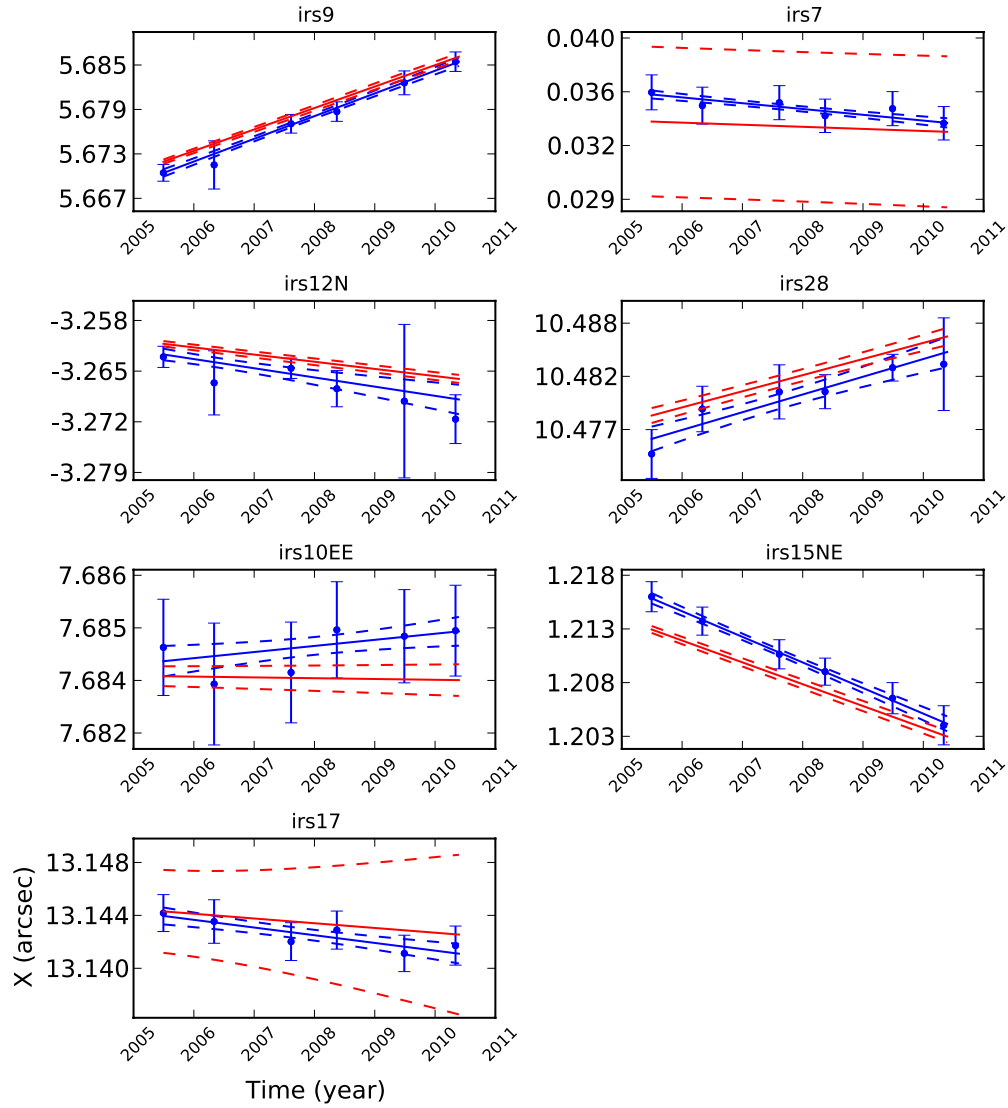


Figure 11. Absolute X positions (where X increases to the east) of GC SiO masers in the infrared as a function of time and the velocity model fit (blue) and the proper motion model for the radio (red). The 1σ errors on the line fits are shown as dashed lines. The IR positional errors shown include centroiding and alignment errors. Radio proper motion measurements are taken from M. Reid (2010, private communication).

reference frame that is more stable than 0.03 mas yr^{-1} (the current limits from the radio measurements alone).

In order to compare the IR and radio positional measurements, two additional steps are required. First, we determine the time, $T_{0,(\text{IR}+\text{radio})}$, at which the positional difference is expected to have the smallest uncertainty for each maser,

$$T_{0,(\text{IR}+\text{radio})} = \frac{\sigma_{v,\text{IR}}^2 T_{0,\text{IR}} + \sigma_{v,\text{radio}}^2 T_{0,\text{radio}}}{\sigma_{v,\text{IR}}^2 + \sigma_{v,\text{radio}}^2}, \quad (3)$$

where $\sigma_{v,\text{IR}}$ and $\sigma_{v,\text{radio}}$ are the velocity errors in the IR and radio, respectively. We take the average of these seven times, 2006.9, and find the IR and radio positions and uncertainties at this common epoch. Then the correlated distortion error (including both the uncertainty in the model and the residual distortion, ~ 0.1 pixel) for each maser is added in quadrature to the formal uncertainty from the infrared fit. Comparison with the radio positions indicates that the position of Sgr A*-radio is known to within $\sim 0.57 \text{ mas}$ in year 2006.9 in our infrared reference frame. We note that the localization of Sgr A*-radio in the IR reference frame is time dependent (Figure 13). Decreasing the

impact of uncertainties in the IR distortion model, with either more highly dithered measurements or a better distortion model, would improve this precision. Overall, our current measurement uncertainties for both the position and velocity of Sgr A* are a factor of 3–4 better than earlier measurements—either those of Ghez et al. (2008), when treated in the same manner,¹⁵ or those reported by Gillessen et al. (2009b) using their “maser system” method, which is comparable to the method used here.^{16,17}

Sgr A* is detected in three of the IR maser mosaics and its position is consistent with Sgr A*-radio in our IR reference frame (Figure 13). In 2008 May, Sgr A* was as bright as

¹⁵ We reported errors from a half-sample bootstrap in Ghez et al. (2008). To compare values, we reran our analysis with the half-sample bootstrap, which overestimates the uncertainties since half the sample is removed.

¹⁶ We note that Gillessen et al. (2009b) derive their astrometry using two distinct methods and adopted the positional errors from one method (the “maser system”) and velocity errors from the second method (the “cluster system”).

¹⁷ The effects of DAR are implicitly corrected for in Gillessen et al. (2009b) through the use of a full first-order transformation (i.e., a six-parameter fit), whereas Ghez et al. (2008) use a four-parameter fit, which cannot fully account for the effects of DAR.

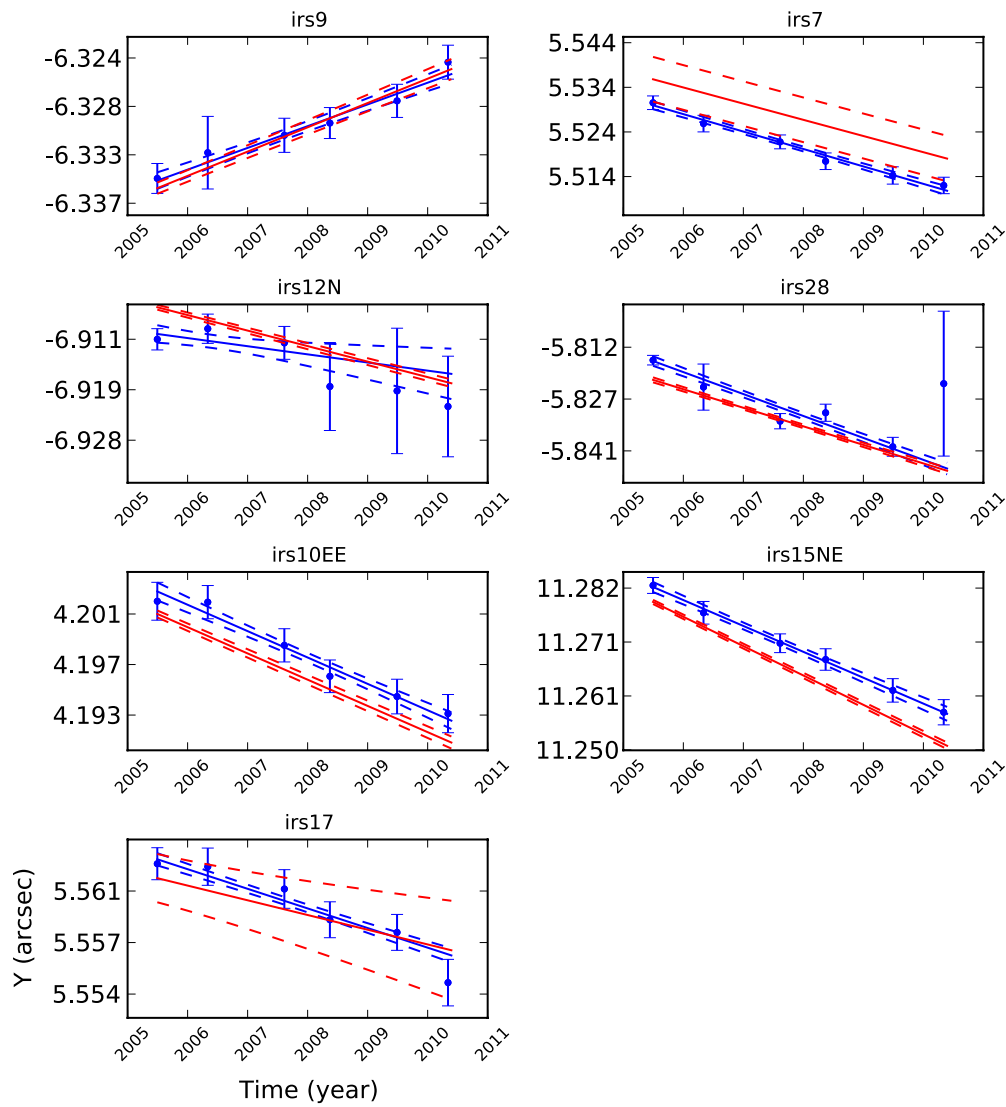


Figure 12. Same as Figure 11 but for Y positions (where Y increases to the north).

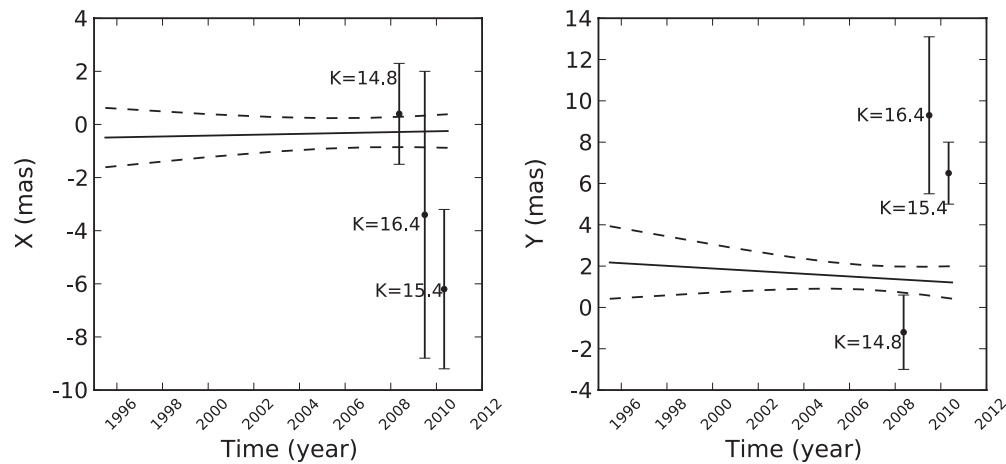


Figure 13. Position of Sgr A*-radio vs. time in the IR reference frame based on analysis in Section 4.1 and values in Table 5 (dotted lines show 1σ uncertainties). Detected positions of Sgr A* in the infrared maser mosaics from 2008 May, 2009 June, and 2010 May are overplotted along with the magnitude of Sgr A*-IR. We note that the fainter detections may suffer from larger astrometric biases from underlying sources. Nonetheless, all three IR positions agree with the radio position of Sgr A*. In the IR reference frame, Sgr A*-radio is consistent with being at rest, at the origin.

$K = 14.8$ mag, which is one of the brightest IR detections of Sgr A* (see, e.g., Do et al. 2009; Sabha et al. 2010). In 2009

June and 2010 May, it was detected with $K = 16.4$ and $K = 15.3$, respectively. The magnitude of Sgr A* in 2009 is more

Table 6
Astrometry of SiO Masers (Polar Coordinates)

Maser	R^a (arcsec)	(IR–Radio) Rad Velocity (mas yr ⁻¹)	(IR–Radio) Tan Velocity (mas yr ⁻¹)	(IR–Radio) Ang Velocity (mas yr ⁻¹ arcsec ⁻¹)
IRS 9	8.503	0.29 ± 0.23 ± 0.12	0.02 ± 0.22 ± 0.11	0.00 ± 0.22 ± 0.11
IRS 7	5.524	-0.28 ± 0.31 ± 0.30	-0.25 ± 0.09 ± 0.22	-0.04 ± 0.09 ± 0.22
IRS 12N	7.644	-1.00 ± 0.96 ± 0.06	0.78 ± 0.62 ± 0.05	0.10 ± 0.62 ± 0.05
IRS 28	11.989	0.60 ± 0.47 ± 0.22	0.75 ± 0.48 ± 0.24	0.06 ± 0.48 ± 0.24
IRS 10EE	8.757	0.15 ± 0.16 ± 0.04	0.09 ± 0.21 ± 0.05	0.01 ± 0.21 ± 0.05
IRS 15NE	11.340	0.64 ± 0.39 ± 0.06	-0.40 ± 0.20 ± 0.05	-0.04 ± 0.20 ± 0.05
IRS 17	14.271	-0.34 ± 0.23 ± 0.94	0.21 ± 0.17 ± 0.63	0.01 ± 0.17 ± 0.63
Weighted average ^b		0.19 ± 0.12	-0.07 ± 0.11	-0.01 ± 0.11

Notes. Infrared (first) and radio (second) formal uncertainties are reported for each maser’s position and velocity.

^a Position reported for the common IR + radio epoch given in Table 5 for each maser, and using proper motions measured in the infrared.

^b Weighted average and error in the weighted average are reported.

in line with the faint end of what is observed for this highly variable source. The later detections were possible because the mosaics were deeper than the previous mosaics. No other mosaics show Sgr A* since these observations are composed of very short exposures to avoid saturation on the infrared-bright SiO masers. Figure 13 shows that all three detections are consistent within 3σ in X and Y with the position of Sgr A*-radio in the IR reference frame. Furthermore, the IR position is more consistent with the radio position (within 1σ) when Sgr A*-IR is in a relatively bright state and less prone to astrometric biases from underlying sources (e.g., Ghez et al. 2008; Gillessen et al. 2009b). This independent comparison confirms that we have a well-constructed reference frame.

By carrying out the same analysis in polar coordinates (as opposed to Cartesian), we find that the infrared and radio Sgr A*-rest coordinate systems show no net relative expansion (V_r) nor rotation (V_t/R) to within 0.12 mas yr^{-1} and $0.11 \text{ mas yr}^{-1} \text{ arcsec}^{-1}$ (1σ), respectively (Table 6).

4.2. Comparison of Sgr A*-Rest Reference Frame and Cluster-Rest Reference Frame

The Sgr A*-rest reference frame generated in Section 4.1 is more stable than the cluster-rest reference frame that has been used as the principle coordinate system for most of the previous proper motion studies. Here we are quantifying frame stability as the uncertainty in the velocity of the object that is defined to be at rest. Since the cluster-rest frame previously used is defined by assuming that a set of reference stars has no net motion, the translational stability of this reference frame is limited to be σ/\sqrt{N} , where σ is the intrinsic dispersion of the stars and N is the number of reference stars used. With a dispersion in the plane of the sky of roughly 3 mas yr^{-1} (Trippe et al. 2008; Schödel et al. 2009; see also Section 4.3), ~ 1100 reference stars would be needed in order to match the stability of our current Sgr A*-rest frame. This is a factor of ~ 2 – 10 more than have been used in earlier studies (e.g., Trippe et al. 2008; Ghez et al. 2008; Lu et al. 2009; Schödel et al. 2009) and comparable to that of Gillessen et al. (2009b).

The stability of reference frames for observations made with fields of view that are too small to tie into the masers directly can be significantly improved by using secondary astrometric standards generated by the proper motion measurements for infrared stars other than the masers from the measurements presented in Section 4.1. To create these secondary standards, we use the same linear motion modeling done for the masers and estimate the positions and proper motions of stars that are

detected in at least four of the six maser mosaics ($N = 1445$). These stars have K' magnitudes that are brighter than 16 mag and a χ^2 distribution that is consistent with their positional uncertainties and degrees of freedom (Figure 14). From these, we select the 1279 stars that have velocities less than 10 mas yr^{-1} (to exclude mismatches) and velocity errors less than 1.5 mas yr^{-1} in both the X and Y directions (Figure 15). The positions and proper motions of these stars are reported in Table 7, and the left panel of Figure 16 shows the cumulative distribution as a function of radius for the entire sample, as well as for those known to be old and young. Reference frames defined based on these secondary astrometric standards (which can be young or old), as opposed to one defined on the premise that the old stars have no net motion, are significantly more stable, and the exact advantage depends on the field coverage; for the Keck speckle and $10'' \times 10''$ AO data (see, e.g., Ghez et al. 2008; Lu et al. 2009), the translational stability is expected to be a factor of 17.5 and 12.5 times better, or 0.03 and 0.02 mas yr^{-1} , respectively (see right panel of Figure 16). Similarly the rotational stability, quantified as the uncertainty in the average rotational velocity, is expected to be a factor of 20 and 9 times better, for the Keck speckle and AO data, or roughly 0.03 and $0.02 \text{ mas yr}^{-1} \text{ arcsec}^{-1}$, respectively. This improvement has been seen and will be presented in a separate forthcoming paper (see also Yelda et al. 2010, conference proceedings showing these results).

4.3. Motion of the Central Stellar Cluster in a Sgr A* Rest Frame

The proper motions for the secondary astrometric standards listed in Table 7 also offer the first opportunity to study the kinematic properties of the central stellar cluster directly in an Sgr A*-rest frame. Since all previous proper motions have been made in the cluster-rest reference frame, any net rotation of the cluster in the plane of the sky is removed from these earlier measurements. Rotationally, we find no motion in the plane of the sky in the tangential velocities ($-0.09 \pm 0.14 \text{ mas yr}^{-1}$) nor in the angular velocities ($0.26 \pm 0.36 \text{ mas yr}^{-1} \text{ arcsec}^{-1}$) about Sgr A* (Figure 17). However, we do detect rotation in the plane of the Galaxy, as has been previously reported by both Trippe et al. (2008) and Schödel et al. (2009) and is shown in Figure 18, which shows that there is a preferred angle for the proper motion vectors of $25^\circ 4 \pm 16^\circ 3$, consistent with the angle of the Galactic plane ($31^\circ 4$; Reid & Brunthaler 2004). This rotation in the Galactic plane is also seen in the flattening of the distribution of velocities in the direction parallel to the Galactic

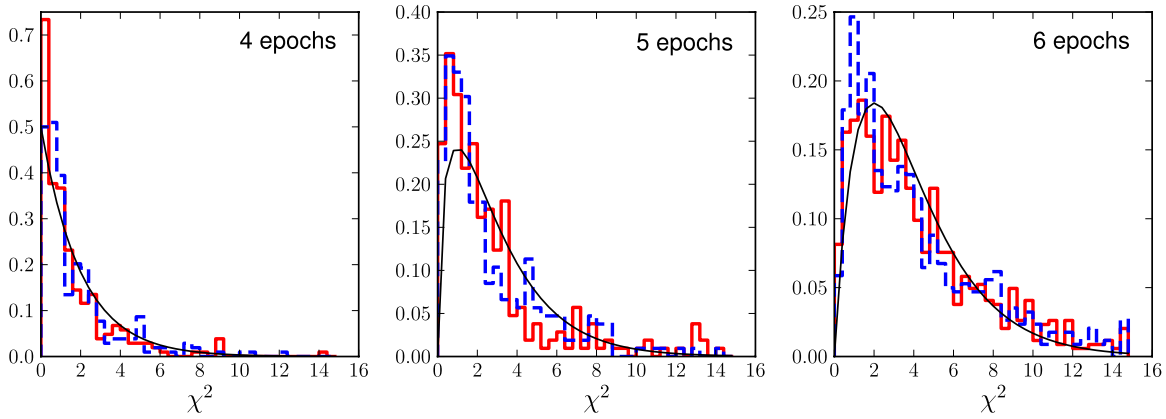


Figure 14. Histogram of velocity χ^2 values in X (solid red) and Y (dashed blue) for the stars detected in four ($N = 263$), five ($N = 269$), and six ($N = 912$) maser mosaics. The theoretical χ^2 distributions for the corresponding degrees of freedom are overlotted as thin black curves for comparison. We find that the velocities are well behaved, as indicated by the similarity between the observed and theoretical distributions.

(A color version of this figure is available in the online journal.)

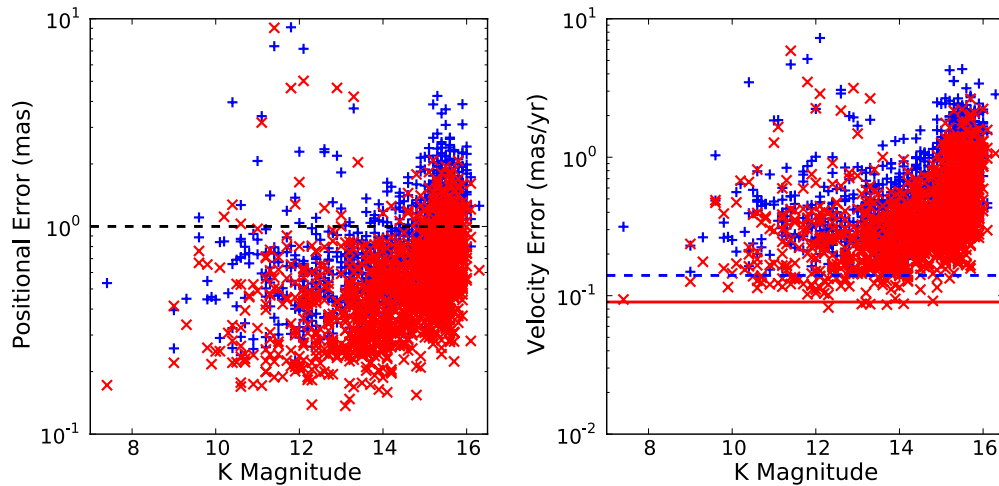


Figure 15. Positional (left) and velocity uncertainties (right) for X (red crosses) and Y (blue plus signs) vs. K magnitude for all stars detected in at least four of the six maser mosaics ($N = 1445$). We select stars with velocities less than 10 mas yr^{-1} and velocity errors less than 1.5 mas yr^{-1} in both the X and Y directions as our infrared astrometric standards, resulting in a total of 1279 stars. The dashed line in the left-hand plot shows the level of residual distortion (1 mas) which is added in quadrature to the positional errors in Table 7. The dashed lines in the right plot indicate the level at which the velocity of Sgr A* is known in the X (solid red) and Y directions (dashed blue), based on the IR to radio offsets of the masers found in Section 4.1 and Table 5.

(A color version of this figure is available in the online journal.)

Table 7
GC Secondary IR Astrometric Standards

Name	K' (mag)	$T_{0,IR}$ (yr)	Radius (arcsec)	Δ R.A. (arcsec)	$\sigma_{R.A.}^a$ (mas)	Δ Decl. (arcsec)	$\sigma_{Decl.}^a$ (mas)	$\nu_{R.A.}^b$ (mas yr $^{-1}$)	$\nu_{Decl.}^b$ (mas yr $^{-1}$)
S0-3	14.8	2008.67	0.36	0.3351	1.4	0.1189	1.4	9.1 ± 0.3	-0.9 ± 0.5
S0-6	14.2	2008.43	0.36	0.0276	1.1	-0.3625	1.2	-5.3 ± 0.1	3.5 ± 0.4
S0-53	15.5	2005.89	0.40	0.3484	1.6	0.2037	1.4	-8.1 ± 1.1	7.5 ± 0.5

Notes.

^a Positional errors include centroiding, alignment, and residual distortion (1 mas) errors, but do not include error in position of Sgr A* (0.55 mas, 0.59 mas in R.A. and decl., respectively).

^b Velocity errors do not include error in velocity of Sgr A* (0.09 mas yr $^{-1}$, 0.14 mas yr $^{-1}$ in R.A. and decl., respectively).

(This table is available in its entirety in a machine-readable form in the online journal. A portion is shown here for guidance regarding its form and content.)

plane as compared to the velocities in the perpendicular direction (Figure 19). Translationally, we find that the weighted average velocity of all the stars in the sample that are not known to be young ($N = 1202$) is $0.21 \pm 0.13 \text{ mas yr}^{-1}$ ($\sim 8.0 \pm 4.9 \text{ km s}^{-1}$ at 8 kpc) and $0.13 \pm 0.14 \text{ mas yr}^{-1}$ ($\sim 4.9 \pm 5.3 \text{ km s}^{-1}$) in the X and Y directions (where X and Y increase to the east and

north), respectively. Figure 20 compares the mean translational motion of the nuclear stellar cluster to the motion of Sgr A* (as determined in Section 4.1) and shows that there is no relative motion between the cluster and the black hole. The uncertainties quoted here are the rms errors of the weighted average velocities from a bootstrap analysis with 10^5 trials, where in each trial a

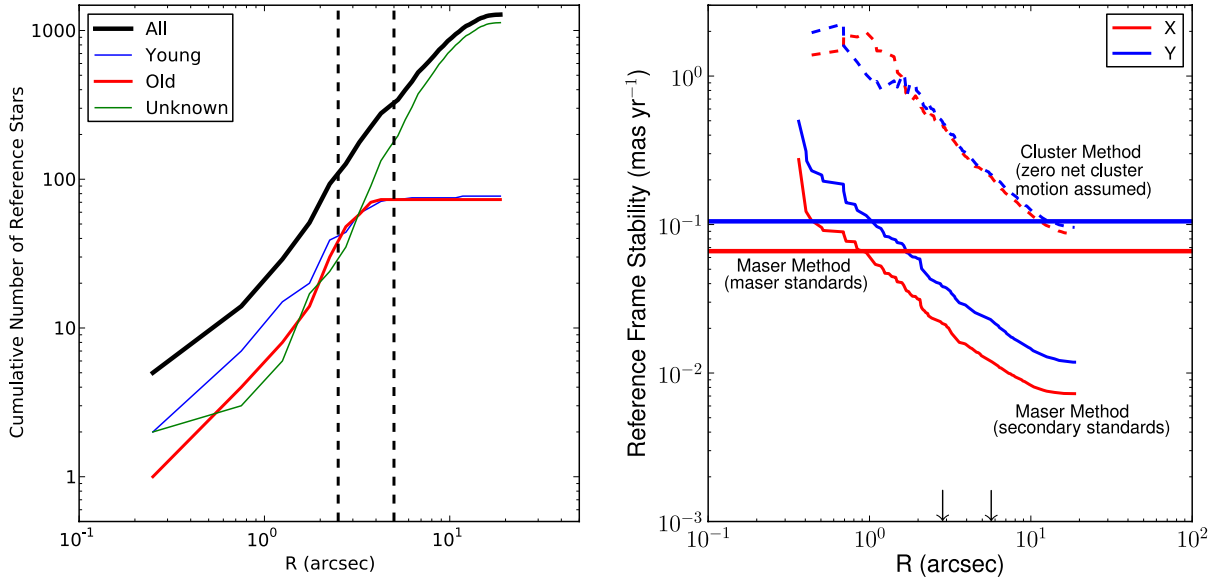


Figure 16. Left: cumulative radial distribution of all 1279 astrometric reference stars (black), as well as the distribution of stars based on spectral identification: young ($N = 77$; blue), old ($N = 73$; red), and unknown ($N = 1129$; green). The field of view for both the speckle ($R = 2.5''$) and the AO ($R = 5''$) cameras is indicated (dashed lines). The speckle data (1995–2005) are dominated by young stars, and thus, using them as reference stars in the coordinate transformations is critical. Stars with unknown spectroscopic identifications dominate at larger radii. Right: error on the weighted average velocity of the cluster stars in X (red) and Y (blue) as a function of distance from Sgr A* as measured using two distinct methods. The curves show the improvement in the errors as more reference stars are included at larger radii. Using the “cluster method” and excluding young stars (dashed curves), the assumption of no net cluster motion is made, resulting in a reference frame that is stable to $\sim 0.2 \text{ mas yr}^{-1}$ at a radius of $5''$ (corresponding to the field of view of Keck AO data). In a reference frame where Sgr A* is at rest, the “maser method,” the error on the weighted average velocity of the cluster stars is $\sim 0.02 \text{ mas yr}^{-1}$ over the extent covered by the AO data (solid curves). The total error in the weighted average velocity from the method described in Section 4.2, which includes contributions from the cluster stars, as well as the masers in both the radio and infrared (horizontal lines), represents the stability of our reference frame (0.09 mas yr^{-1}).

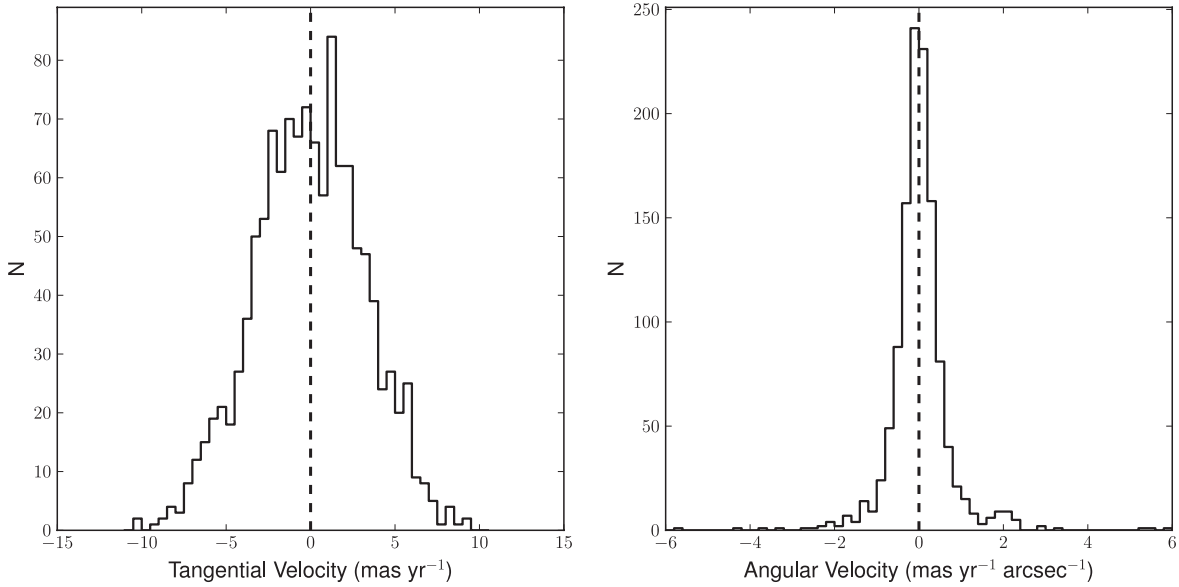


Figure 17. Left: histogram of tangential velocities of the astrometric reference stars (excluding known young stars). The tangential motion in the plane of the sky is consistent with zero mas yr^{-1} (dashed line). Right: histogram of angular velocities of the reference stars (excluding known young stars). The angular velocity is consistent with zero $\text{mas yr}^{-1} \text{ arcsec}^{-1}$ (dashed line).

random set of data was sampled (with replacement) from the observed cluster velocity distribution.

5. SUMMARY AND CONCLUSIONS

We have improved upon existing geometric distortion solutions for the NIRC2 camera at the W. M. Keck II telescope and have, for the first time, implemented DAR corrections to our GC

astrometry. In all tests that were performed, the new distortion solution shows an improvement by a factor of $\sim 2\text{--}4$ over existing solutions. We take as our final residuals: $(\sigma_x, \sigma_y) \sim (0.11, 0.10) \text{ pixel} \sim (1.1, 1.0) \text{ mas}$. This is the error that is incurred when combining images taken at various offsets and P.A.s. The transformations between the ACS/WFC and NIRC2 reference frames yield a consistent plate scale and angle offset to that obtained using GC infrared data which are tied to the radio

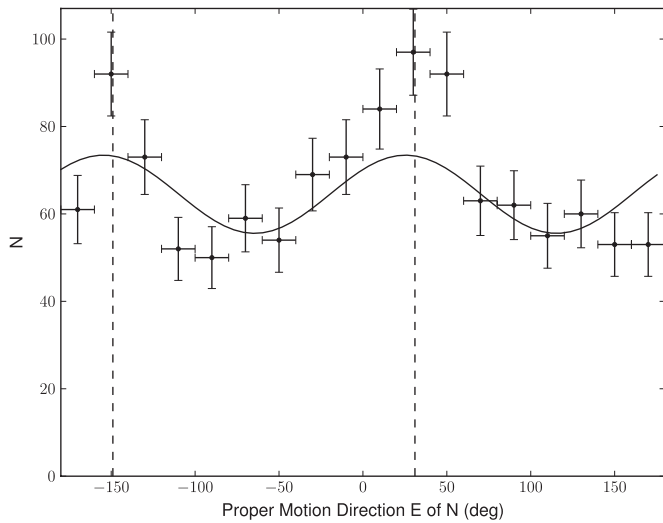


Figure 18. Histogram of proper motion direction, defined as the angle east of north, of the infrared astrometric standards in the central ~ 1 pc. The vertical error bars are Poisson errors, while the horizontal bars denote the width of the histogram bins. The angle of the Galactic plane is shown as the dashed line ($\sim 31^\circ$ and 180° opposite). The data are best fit with a cosine curve which peaks at 25.4 ± 16.3 , which is consistent with the angle of the Galactic plane.

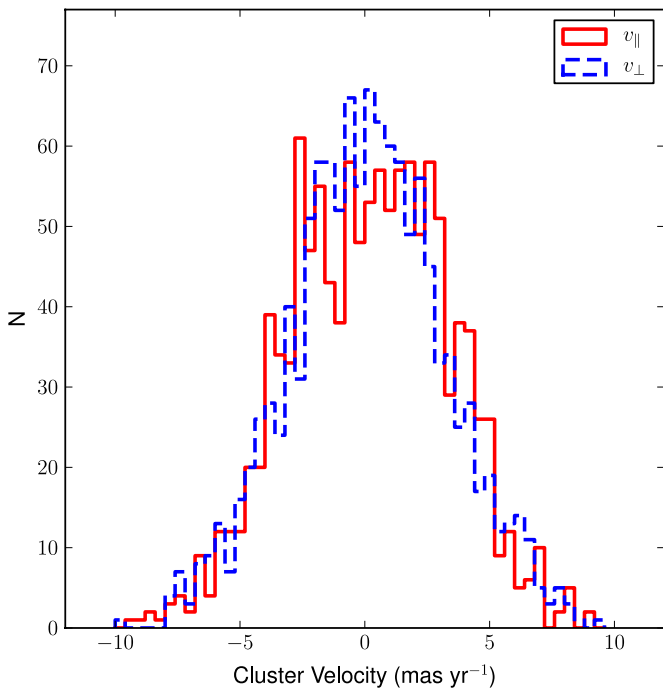


Figure 19. Reference star velocities parallel (solid red) and perpendicular (dashed blue) to the Galactic plane ($\theta = 31.4^\circ$). The flattening of the v_{\parallel} distribution is due to the rotation of the cluster stars along the Galactic plane. (A color version of this figure is available in the online journal.)

reference frame. We find an average plate scale and angle offset for the NIRC2 narrow camera of 9.952 ± 0.002 mas pixel $^{-1}$ and 0.252 ± 0.009 , respectively.

The new distortion solution and its associated uncertainty, in the form of FITS files.¹⁸ The FITS files, or look-up tables, may be fed into the IRAF routine *Drizzle* during the data reduction process. The values in the look-up tables specify the shifts required to put an image into a “distortion-free” reference frame.

¹⁸ <http://www.astro.ucla.edu/~ghezgroup/distortion>

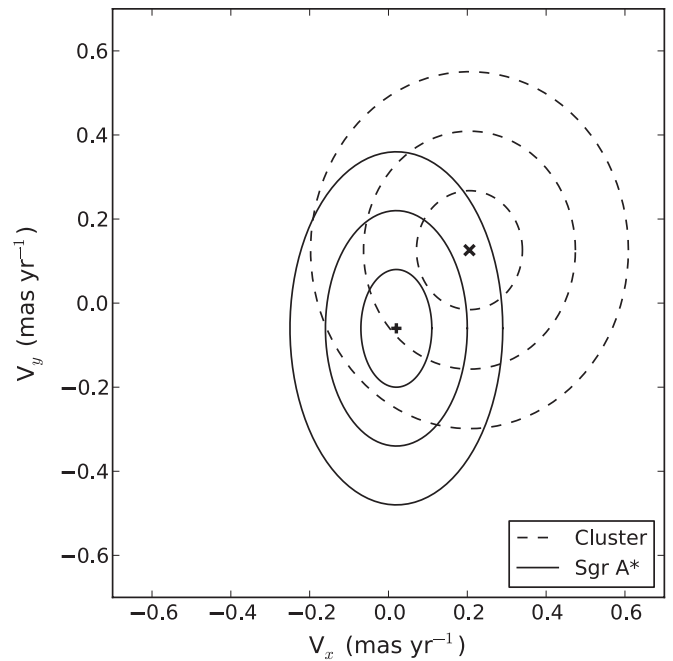


Figure 20. Velocity of Sgr A* in the infrared reference frame (plus sign) with 1σ , 2σ , and 3σ contours shown (solid curves), as compared to the cluster’s weighted average velocity (cross; dashed curves). V_x and V_y are defined such that positive values are motions that increase in the east and north directions, respectively.

As a result of the work presented here, GC astrometry can now be tied to an Sgr A*-radio rest frame to better than ~ 0.6 mas and ~ 0.1 mas yr $^{-1}$ (~ 3.5 km s $^{-1}$ at 8 kpc) in position and velocity space, respectively, which is a factor of 3 improvement over earlier reported efforts. We note that the velocity of Sgr A* along the line of sight is likely to be minimal (~ 3.5 km s $^{-1}$, 1σ) given the constraints on the motion in the plane of the sky. Since the cluster has been found to exhibit no net motion with respect to the local standard of rest (LSR) to within ± 5 km s $^{-1}$ (Figer et al. 2003; Trippe et al. 2008), this adds confidence in the estimates of the distance to the GC (R_o) from orbital analyses in which the black hole is assumed to have no line-of-sight motion with respect to the LSR. With this assumption, R_o estimates from comparable orbital analyses in Ghez et al. (2008), Gillessen et al. (2009a), and Gillessen et al. (2009b) have values of 8.4 ± 0.4 kpc, 7.7 ± 0.4 kpc, and 7.3 ± 0.5 kpc, respectively.¹⁹

We present a new set of infrared astrometric standards that can be used to define the reference frame (with Sgr A*-radio at rest, at the origin) in smaller field of view GC measurements that do not contain enough of the SiO radio masers and that are used for stellar orbit measurements. We measure the motion of the stellar cluster in an Sgr A*-rest frame and confirm that the cluster rotates in the plane of the Galaxy.

A stable astrometric reference frame is a key requirement when using stellar orbits to study the central supermassive black hole and its environment. Stellar orbits have already proven to be powerful tools for measuring the black hole’s mass and distance, as well as placing limits on a black hole companion (Ghez et al. 2008; Gillessen et al. 2009b). In time, stellar orbital work will probe the extended mass distribution and general relativity through the detection of prograde and retrograde

¹⁹ The orbital analysis compared is the case of S0-2 only, no 2002 astrometric data, and priors only on V_z .

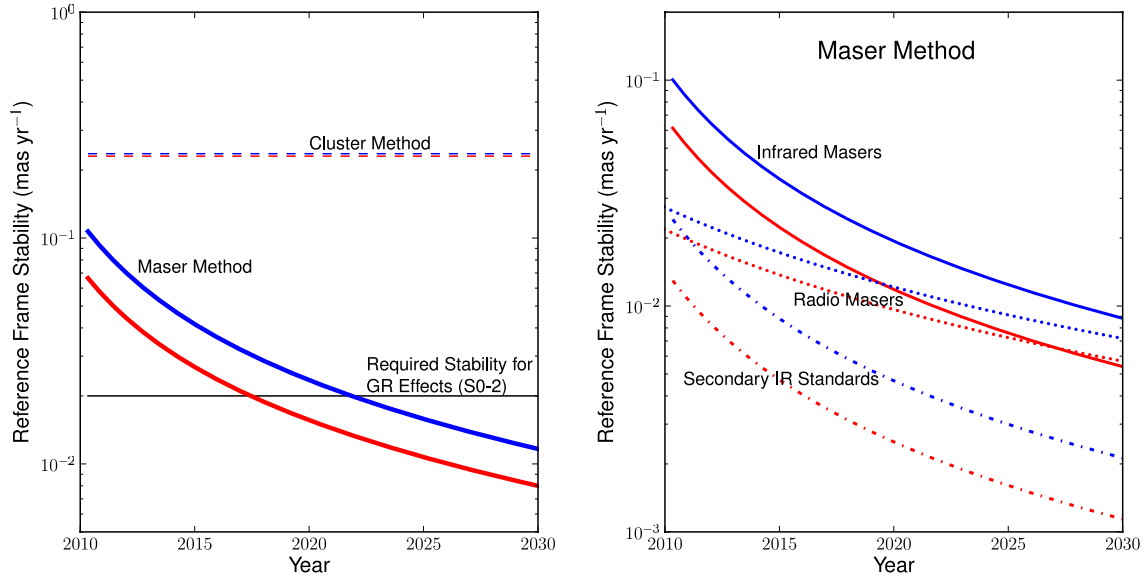


Figure 21. Left: predicted stability in X (red) and Y (blue) of the reference frame with time (assuming the field of view of Keck AO images, $10'' \times 10''$). The maser method (solid curves; Section 4) allows for an improvement in the stability with time as $t^{-3/2}$, whereas the cluster method (dashed lines), which assumes no net motion of the stellar cluster, is fundamentally limited by the cluster’s intrinsic dispersion and therefore will not improve with time. In order to detect the prograde relativistic precession at the 3σ level (neglecting the retrograde precession due to the extended mass distribution), the reference frame must be stable to within $\sim 0.02 \text{ mas yr}^{-1}$ (black line). Using the maser method, a significant detection of the retrograde precession of S0–2’s orbit will be possible beginning in the year ~ 2022 . Right: the three sources of error that contribute to the stability of the reference frame using the maser method are shown separately. These include the radio masers (dotted), the infrared masers (thick solid), and the secondary astrometric standards (dash-dotted). Note the different scaling for the Y axis in the two plots.

precession, respectively (Rubilar & Eckart 2001). Weinberg et al. (2005) considered the effect of an assumed extended mass distribution within the orbit of the central arcsecond, 16 year period star, S0–2, and estimated an apocenter shift after one revolution of $\Delta s \sim 0.3 \text{ mas}$, which corresponds to an effect of $\phi \sim 0.02 \text{ mas yr}^{-1}$ (or an angular velocity of $0.08 \text{ mas yr}^{-1} \text{ arcsec}^{-1}$).²⁰ The prograde relativistic precession of S0–2, on the other hand, is predicted to be $\phi \sim 0.06 \text{ mas yr}^{-1}$ (or an angular velocity of $0.27 \text{ mas yr}^{-1} \text{ arcsec}^{-1}$; Weinberg et al. 2005), thereby requiring a reference frame that is stable to 0.02 mas yr^{-1} . Detection of either the prograde or the retrograde precession of the central arcsecond sources will therefore require an extremely stable astrometric reference frame.

Figure 21 shows the expected improvement in the stability of the astrometric reference frame with time using the maser method described in Section 4. The various contributions to the stability of the reference frame come from measurements of the SiO masers in both the radio (dotted lines) and infrared (dash-dotted lines), as well as from the transformation of the infrared stars into the Sgr A*-radio rest frame (thick solid lines). In order to detect either the prograde relativistic precession or the retrograde precession from the extended mass distribution, the combination of these various sources of error must be reduced to less than 0.02 mas yr^{-1} . Figure 21 shows that this will be possible only starting in the year ~ 2022 , using the method described in Section 4. High precision radio measurements of additional masers within this region, such as IRS 14NE (Li et al. 2010) or others that may be discovered with the Expanded Very Large Array (EVLA), would help to achieve the required level of precision more rapidly, as the IR measurements are already in hand for this entire region.

We thank the staff of the Keck Observatory, especially Randy Campbell, Al Conrad, Jim Lyke, and Hien Tran for their help

²⁰ We note that this is only an approximation as the amount of extended mass within the orbit of S0–2 is highly unknown.

in obtaining the observations. We are grateful to Mark Reid for providing the latest VLA measurements of the Galactic center. We also thank Mark Morris, Quinn Konopacky, Marshall Perrin, and Leo Meyer for their helpful suggestions on this work and the manuscript. Support for this work was provided by the NSF grants AST-0406816 and AST-0909218 and the NSF Science & Technology Center for Adaptive Optics, managed by UCSC (AST-9876783). The W. M. Keck Observatory is operated as a scientific partnership among the California Institute of Technology, the University of California, and the National Aeronautics and Space Administration. The Observatory was made possible by the generous financial support of the W. M. Keck Foundation. The authors also recognize and acknowledge the very significant cultural role and reverence that the summit of Mauna Kea has always had within the indigenous Hawaiian community. We are most fortunate to have the opportunity to conduct observations from this mountain.

Facilities: Keck: II (NIRC2)

APPENDIX A

STARFINDER

StarFinder iteratively determines first the PSF, from a set of user-selected “PSF stars,” and then the positions and fluxes of all stars in the field (Diolaiti et al. 2000). Successive iterations improve the PSF estimate by subtracting off stars identified in the previous pass. However, errors in the initial PSF estimate can lead to spurious source detections due to speckles or airy ring substructure that are incorrectly identified as stars. These errors propagate through all iterations and lead to increased astrometric noise from fitting an incorrect PSF and astrometric biases due to the detection of false sources.

To minimize the impact of these false sources on the PSF estimation and subsequent astrometry and photometry, we insert a step into each *StarFinder* iteration that trims out these false sources from the list of identified stars before re-extracting the

PSF on subsequent iterations. We define our valid star detection limits as a contrast curve of delta-magnitude versus separation, which is computed by azimuthally averaging the PSF. For every source, we remove all detections that are fainter than this contrast curve. This typically removes 20% of the originally detected sources, with roughly half coming from substructure in the first airy wing and the other half coming from speckles in the extended PSF halo. We also increased our PSF box size from $1''$, as used in Ghez et al. (2008) and Lu et al. (2009), to $2''$ to improve photometric accuracy; however, this had a minimal impact on astrometry.

APPENDIX B

DISTORTION UNCERTAINTIES FOR THE IR MASER MOSAIC

We generate a map of positional uncertainties that arise from uncertainties in the distortion model for our IR maser mosaic to facilitate assignment of this source of uncertainty. This is simply a mosaic of the distortion uncertainty models discussed in Section 3.1 and shown in Figure 7, where the residual distortion of 0.1 pixel (Section 3.2) was added in quadrature to each pixel. To construct the mosaicked error map, we compute the distortion error contribution at each pixel as

$$\sigma_{\text{dist}} = \sqrt{\frac{\sigma_1^2 + \sigma_2^2 + \dots + \sigma_N^2}{N}}, \quad (\text{B1})$$

where σ_i is the distortion uncertainty at each individual pixel and N is the number of overlapping fields, which can vary between 1 and 4. This resulted in a mosaicked map of approximately 2200×2200 pixel.

APPENDIX C

POSSIBLE ASTROMETRIC BIAS FROM IRS 7

The linear motion modeling of the IR maser measurements in Section 4.1 has unexpectedly low reduced χ^2 . In our current analysis, alignment uncertainties are treated as purely random errors. If there is a systematic problem with one of the radio maser positions, this could create a significant correlated alignment error that is not captured in our present analysis and cause the reduced χ^2 to be smaller than its expected value for random errors. Indeed, one possible culprit is the radio position of IRS 7, which, as discussed in Reid et al. (2003), is more uncertain than the other masers used for two related reasons. First, it is a supergiant and therefore is expected to have a much larger maser emission region ($r \sim 10$ mas) than the other masers used, which are thought to be Mira variables ($r \sim 1$ mas). Second, the maser spot location for IRS 7 jumped in 1998 (although the spots moved with similar proper motion before and after 1998), making the position of IRS 7 harder to assess than its proper motion. The solution has been to take the mid-point between the positions before and after 1998, which amounts to applying a 10 mas offset to the post-1998 values and increasing the positional uncertainties to 5 mas. If we remove this offset from the reported position of IRS 7 in our analysis (prior to aligning the IR positions in each epoch), the resulting average χ^2 of the linear motion models for the IR maser measurements is 0.97,

which may suggest that this offset should not be applied. Since this has only a minor impact on our current analysis, we have used the values reported in Section 4.1 and Table 5 for the results reported in this study. However, this may become a more important issue in the future as the precision of the IR maser measurements improves as discussed in Section 5.

REFERENCES

- Anderson, J. 2005, in *The 2005 HST Calibration Workshop Proc.*, ed. A. Koekemoer, P. Goudfrooij, & L. L. Dressel (Baltimore, MD: STScI), 11
- Anderson, J. 2007, Instrument Science Report ACS 2007–08
- Anderson, J., & King, I. R. 2006, Instrument Science Report ACS 2006–01
- Anderson, J., et al. 2008, *AJ*, **135**, 2055
- Cameron, P. B., & Kulkarni, S. R. 2007, *BAAS*, **38**, 996
- Dierckx, P. 1995, *Curve and Surface Fitting with Splines* (Oxford: Clarendon Press)
- Diolaiti, E., Bendinelli, O., Bonaccini, D., Close, L., Currie, D., & Parmeggiani, G. 2000, *A&AS*, **147**, 335
- Do, T., Ghez, A. M., Morris, M. R., Yelda, S., Meyer, L., Lu, J. R., Hornstein, S. D., & Matthews, K. 2009, *ApJ*, **691**, 1021
- Dupuy, T. J., Liu, M. C., & Ireland, M. J. 2009, *ApJ*, **699**, 168
- Eckart, A., & Genzel, R. 1997, *MNRAS*, **284**, 576
- Figer, D. F., et al. 2003, *ApJ*, **599**, 1139
- Fragile, P. C., & Mathews, G. J. 2000, *ApJ*, **542**, 328
- Fruchter, A. S., & Hook, R. N. 2002, *PASP*, **114**, 144
- Genzel, R., et al. 2003, *ApJ*, **594**, 812
- Ghez, A. M., Klein, B. L., Morris, M., & Becklin, E. E. 1998, *ApJ*, **509**, 678
- Ghez, A. M., et al. 2008, *ApJ*, **689**, 1044
- Gillessen, S., Eisenhauer, F., Fritz, T. K., Bartko, H., Dodds-Eden, K., Pfuhl, O., Ott, T., & Genzel, R. 2009a, *ApJ*, **707**, L114
- Gillessen, S., Eisenhauer, F., Trippe, S., Alexander, T., Genzel, R., Martins, F., & Ott, T. 2009b, *ApJ*, **692**, 1075
- Gubler, J., & Tytler, D. 1998, *PASP*, **110**, 738
- Jaroszynski, M. 1998, *Acta Astron.*, **48**, 413
- Jaroszynski, M. 1999, *ApJ*, **521**, 591
- Konopacky, Q. M., Ghez, A. M., Duchêne, G., McCabe, C., & Macintosh, B. A. 2007, *AJ*, **133**, 2008
- Kraniotis, G. V. 2007, *Class. Quantum Grav.*, **24**, 1775
- Levin, Y., & Beloborodov, A. M. 2003, *ApJ*, **590**, L33
- Li, J., An, T., Shen, Z., & Miyazaki, A. 2010, *ApJ*, **720**, L56
- Liu, M. C., Dupuy, T. J., & Ireland, M. J. 2008, *ApJ*, **689**, 436
- Lu, J. R. 2008, PhD thesis, UCLA
- Lu, J. R., Ghez, A. M., Hornstein, S. D., Morris, M. R., Becklin, E. E., & Matthews, K. 2009, *ApJ*, **690**, 1463
- Marois, C., Macintosh, B., Barman, T., Zuckerman, B., Song, I., Patience, J., Lafrenière, D., & Doyon, R. 2008, *Science*, **322**, 1348
- Max, C. E., Canalizo, G., Macintosh, B. A., Raschke, L., Whysong, D., Antonucci, R., & Schneider, G. 2005, *ApJ*, **621**, 738
- Nucita, A. A., De Paolis, F., Ingrosso, G., Qadir, A., & Zakharov, A. F. 2007, *PASP*, **119**, 349
- Paumard, T., et al. 2006, *ApJ*, **643**, 1011
- Reid, M. J., & Brunthaler, A. 2004, *ApJ*, **616**, 872
- Reid, M. J., Menten, K. M., Genzel, R., Ott, T., Schödel, R., & Eckart, A. 2003, *ApJ*, **587**, 208
- Reid, M. J., Menten, K. M., Trippe, S., Ott, T., & Genzel, R. 2007, *ApJ*, **659**, 378
- Rubilar, G. F., & Eckart, A. 2001, *A&A*, **374**, 95
- Sabha, N., et al. 2010, *A&A*, **512**, A2
- Salim, S., & Gould, A. 1999, *ApJ*, **523**, 633
- Schödel, R., Merritt, D., & Eckart, A. 2009, *A&A*, **502**, 91
- Stolte, A., Ghez, A. M., Morris, M., Lu, J. R., Brandner, W., & Matthews, K. 2008, *ApJ*, **675**, 1278
- Trippe, S., et al. 2008, *A&A*, **492**, 419
- van der Marel, R. P., Anderson, J., Cox, C., Kozhurina-Platais, V., Lallo, M., & Nelan, E. 2007, Instrument Science Report ACS 2007–07
- Weinberg, N. N., Milosavljević, M., & Ghez, A. M. 2005, *ApJ*, **622**, 878
- Will, C. M. 2008, *ApJ*, **674**, L25
- Yelda, S., Ghez, A. M., Lu, J. R., Do, T., Clarkson, W., & Matthews, K. 2010, arXiv:1002.1729
- Zucker, S., & Alexander, T. 2007, *ApJ*, **654**, L83